PLOS BIOLOGY

RESEARCH ARTICLE

ADAMTS13 maintains cerebrovascular integrity to ameliorate Alzheimer-like pathology

Yongliang Cao[1☯], Haochen Xu[1☯], Yuanbo Zhu[1☯], Mei-Juan Shi[1], Lixiang Wei[1], Jin Zhang[2], Shuo Cheng[1], Yiqian Shi[1], Haiyang Tong[2], Lijing Kang[1], Lu Lu[1], Haiyu Luo[1], Xing Yang[1], Xiaofei Bai[1], Ranran Wang[1], Yuanyuan Ma[1], Yun Wang[1], Zhongfeng Wang[1], Kai Zhong[2,3]*, Bing-Qiao Zhao[1]*, Wenying Fan[1]*

1 Department of Translational Neuroscience, Jingâ an District Centre Hospital of Shanghai, State Key Laboratory of Medical Neurobiology and MOE Frontiers Center for Brain Science, Institutes of Brain Science, Fudan University, Shanghai, China, **2** High Magnetic Field Laboratory, Hefei Institutes of Physical Science, Chinese Academy of Sciences, Anhui, China, **3** Neurodegenerative Disease Research Center, School of Life Sciences, University of Science and Technology of China, CAS Key Laboratory of Brain Functions and Disease, Hefei, China

☯ These authors contributed equally to this work.
* wenyingf@fudan.edu.cn (WF); bingqiaoz@fudan.edu.cn (BQZ); kzhong@hmfl.ac.cn (KZ)

Citation: Cao Y, Xu H, Zhu Y, Shi M-J, Wei L, Zhang J, et al. (2019) ADAMTS13 maintains cerebrovascular integrity to ameliorate Alzheimer-like pathology. PLoS Biol 17(6): e3000313. https://doi.org/10.1371/journal.pbio.3000313

Academic Editor: Richard Daneman, UCSD, UNITED STATES

Received: June 27, 2018

Accepted: May 21, 2019

Published: June 11, 2019

Data Availability Statement: All relevant data are within the paper and its Supporting Information files.

Funding: This work was supported by grants from the National Natural Science Foundation of China (Key Program 81530034 (B.Q.Z.), General Program 81671156 (W.F.) and 81471331 (W.F.)), the National Key Research and Development Program of China, Ministry of Science and

Abstract

Blood-brain barrier (BBB) defects and cerebrovascular dysfunction contribute to amyloid-β (Aβ) brain accumulation and drive Alzheimer disease (AD) pathology. By regulating vascular functions and inflammation in the microvasculature, a disintegrin and metalloprotease with thrombospondin type I motif, member 13 (ADAMTS13) plays a significant protective effect in atherosclerosis and stroke. However, whether ADAMTS13 influences AD pathogenesis remains unclear. Using in vivo multiphoton microscopy, histological, behavioral, and biological methods, we determined BBB integrity, cerebrovascular dysfunction, amyloid accumulation, and cognitive impairment in *APPPS1* mice lacking ADAMTS13. We also tested the impact of viral-mediated expression of ADAMTS13 on cerebrovascular function and AD-like pathology in *APPPS1* mice. We show that ADAMTS13 deficiency led to an early and progressive BBB breakdown as well as reductions in vessel density, capillary perfusion, and cerebral blood flow in *APPPS1* mice. We found that deficiency of ADAMTS13 increased brain plaque load and Aβ levels and accelerated cerebral amyloid angiopathy (CAA) by impeding BBB-mediated clearance of brain Aβ, resulting in worse cognitive decline in *APPPS1* mice. Virus-mediated expression of ADAMTS13 attenuated BBB disruption and increased microvessels, capillary perfusion, and cerebral blood flow in *APPPS1* mice already showing BBB damage and plaque deposition. These beneficial vascular effects were reflected by increase in clearance of cerebral Aβ, reductions in Aβ brain accumulation, and improvements in cognitive performance. Our results show that ADAMTS13 deficiency contributes to AD cerebrovascular dysfunction and the resulting pathogenesis and cognitive deficits and suggest that ADAMTS13 may offer novel therapeutic opportunities for AD.

Technology of China (2016YFC1300500-501 (B.Q. Z.) and 2016YFC1300500-502 (W.F.)) and the Natural Science Foundation of Shanghai (14ZR1401800 (W.F.).

Competing interests: The authorshave declared that no competing interests exist.

Abbreviations: AAV8, adeno-associated virus serotype 8; AD, Alzheimer disease; ADAMTS13, a disintegrin and metalloprotease with thrombospondin type I motif, member 13; APP, amyloid precursor protein; Aβ, amyloid-β; α-CTF, APP C-terminal fragment; BACE1, β-secretase; BBB, blood-brain barrier; β-CTF, BACE1 C-terminal fragment; CAA, cerebral amyloid angiopathy; CA1, field CA1 of hippocampus; CD31, platelet endothelial cell adhesion molecule-1; CMV, cytomegalovirus; ELISA, enzyme-linked immunosorbent assay; FAM-Aβ42, Aβ1–42 labeled with 5(6)-carboxyfluorescein; FITC, fluorescein isothiocyanate; GFAP, glial fibrillary acidic protein; hCMEC/D3, human cerebral microvascular endothelial; HFIP, 1,1,1,3,3,3-hexafluoro-2-propanol; HJ5.1, Aβ-stabilizing anti-Aβ antibody HJ5.1; LRP1, lipoprotein receptor-related protein 1; mEPSC, miniature excitatory postsynaptic current; MW, molecular weight; MWM, Morris water maze; P-gp, P-glycoprotein; PS, permeability surface; PS1, presenilin 1; rADAMTS13, recombinant ADAMTS13; RAGE, receptor for advanced glycation end products; RFP, red fluorescent protein; RT-PCR, reverse transcription-Polymerase Chain Reaction; ThS, thioflavin S; TMR, Tetramethylrhodamine; UL-VWF, ultralarge VWF; VE, vascular endothelial-cadherin; VWF, von Willebrand factor; WT, wild type; ZO-1, Zonula Occludens-1.

Introduction

Alzheimer disease (AD) is associated with distinct cerebrovascular abnormalities and cerebral accumulation of amyloid-β peptide (Aβ) [1,2]. In the AD brain, blood-brain barrier (BBB) breakdown and cerebrovascular dysfunction have been suggested to contribute to the pathology and cognitive deficits [3,4].

von Willebrand factor (VWF) is a large multimeric glycoprotein that is elevated during aging and in patients with vascular dementia [5,6,7]. The multimeric size of VWF is regulated by a disintegrin and metalloprotease with thrombospondin type I motif, member 13 (ADAMTS13), which processed proteolytically VWF into smaller and less reactive fragments [8]. ADAMTS13 deficiency results in ultralarge VWF (UL-VWF) multimers in the circulation, causing vascular dysfunction and inflammation in the microvasculature [9,10]. A reduced plasma ADAMTS13 activity and increased VWF levels are associated with an increased risk of cardiovascular and cerebrovascular diseases, such as atherosclerosis, stroke, and vascular remodeling [11–14]. In experimental animal models, VWF was reported to release upon endothelium injury and promote vascular leakage [15,16], whereas ADAMTS13 protected the BBB integrity by enhancing VWF cleavage [16,17]. However, whether the ADAMTS13-VWF axis can modulate cerebrovascular functions influencing AD pathology remains unclear.

An early BBB breakdown and microvascular reduction have been demonstrated in AD patients [18,19]. Increasing evidence also suggests that neurovascular dysfunction is critical for Aβ accumulation in blood vessels and parenchyma of the brain of AD patients and its associated dementia [1,2,4]. Because deficiency of ADAMTS13 leads to increased VWF-dependent vascular dysfunction [17,20,21], we hypothesized that ADAMTS13 may improve cerebrovascular pathologies associated with Aβ accumulation and cognitive impairment.

To address this issue, we investigated the effect of ADAMTS13 deletion on BBB integrity, cerebrovascular degeneration, Aβ deposition, and cognitive function in mice expressing mutant forms of amyloid precursor protein (APP) and presenilin 1 (PS1). We also evaluated the efficacy of virus-mediated expression of ADAMTS13 on vascular dysfunction, AD pathogenesis, and cognitive deficits in *APPPS1* mice.

Results

Characterization of *APPPS1* and *APPPS1–Adamts13*$^{-/-}$ mice

To examine the levels of human APP in brains of transgenic mice, we subjected brain homogenates to immunoblot analyses using the human-Aβ-specific antibody 6E10 [22,23]. The presence of full-length 100/105 kDa human APP can only be seen in homogenates from *APPPS1* and *APPPS1–Adamts13*$^{-/-}$ mice (S1A Fig). Immunoblot analyses with the antibody that recognizes both human and mouse APP indicated a marked increase in APP protein expression in the brains of transgenic mice compared with nontransgenic mice (S1B Fig). Immunoblot probed with antibody to the C-terminal loop domain revealed the full-length human PS1 (S1C Fig, filled arrow) and the human C-terminal fragments (S1C Fig, open arrow) in the brains of transgenic mice [24]. Disruption of ADAMTS13 was confirmed by PCR (S1D Fig), and ADAMTS13 mRNA was detected by reverse transcription-Polymerase Chain Reaction (RT-PCR) in the liver of (wild-type) WT and *APPPS1* mice but not in *APPPS1–Adamts13*$^{-/-}$ mice (S1E Fig).

ADAMTS13 activities and VWF levels in plasma

We analyzed mice for plasma ADAMTS13 activity. We found a significant reduction in plasma ADAMTS13 activity in 12-month-old *APPPS1* mice compared with age-matched WT mice

and 2- and 6-month-old *APPPS1* mice (Fig 1A). A slight but not statistically significant decrease in ADAMTS13 activity was observed in 6-month-old *APPPS1* mice compared with 2-month-old *APPPS1* mice, suggesting a reduction of ADAMTS13 activity with age in *APPPS1* mice. Because the only known substrate for ADAMTS13 is VWF [9], we analyzed plasma VWF levels. This analysis indicated that *Adamts13*$^{-/-}$ and *APPPS1–Adamts13*$^{-/-}$ mice at 2, 6, and 12 months of age exhibited greater increases in plasma VWF levels compared with age-matched WT and *APPPS1* mice (Fig 1B). Deficiency of ADAMTS13 in *APPPS1* mice resulted in an age-dependent increase in plasma VWF levels. Plasma VWF levels also were significantly increased in 12-month-old *APPPS1* mice compared with age-matched WT mice and 2-month-old *APPPS1* mice. Moreover, we observed a marked increase in the ratio of plasma UL-VWF to low–molecular-weight VWF multimers in 12-month-old *APPPS1–Adamts13*$^{-/-}$ mice compared with age-matched *APPPS1* littermates (Fig 1C and 1D).

ADAMTS13 deficiency leads to early and progressive BBB breakdown in *APPPS1* mice

We quantified BBB permeability by in vivo multiphoton imaging assays of a vascular tracer, fluorescein isothiocyanate (FITC)-dextran (molecular weight (MW) = 40,000 Da). In contrast to the intact BBB observed in 2-month-old WT, *Adamts13*$^{-/-}$, or *APPPS1* mice, the BBB was leaky in age-matched *APPPS1–Adamts13*$^{-/-}$ littermate mice (Fig 2A and 2C). Similarly, immunostaining of fibrin with platelet endothelial cell adhesion molecule-1 (CD31) showed significant perivascular fibrin deposits in the hippocampus and cortex of 2-month-old *APPPS1–Adamts13*$^{-/-}$ mice (Fig 2B and 2D and S2A Fig). Additionally, immunoblot analysis of fibrin in capillary-depleted brain tissue revealed that fibrin accumulated significantly in the brain parenchyma of 2-month-old *APPPS1–Adamts13*$^{-/-}$ mice but not in WT, *Adamts13*$^{-/-}$, or *APPPS1* littermate mice (S2B and S2C Fig). Multiphoton microscopy analysis of FITC-dextran leakage and quantification of perivascular fibrin deposits indicated that BBB permeability increased with increasing age in *APPPS1–Adamts13*$^{-/-}$ mice (Fig 2A, 2B, 2C and 2D and S2A, S2B and S2C Fig). *APPPS1* mice showed increased BBB permeability at 12 months of age, consistent with earlier reports that BBB breakdown was present in this transgenic mice at 9 to 12 months of age [19,25–27]. However, in *APPPS1–Adamts13*$^{-/-}$ mice, the brains were substantially more permeable at this age. Together, these data indicate that ADAMTS13 deletion is sufficient to induce early and progressive BBB damage in *APPPS1* mice.

To investigate whether the BBB breakdown could be related to altered endothelial junctions, we analyzed the expression of junctional proteins in *APPPS1–Adamts13*$^{-/-}$ mice. Immunoblotting showed progressive age-dependent loss of the tight junction protein Zonula Occludens-1 (ZO-1) and the adherens junction protein vascular endothelial-cadherin (VE-cadherin) in isolated brain capillaries of *APPPS1–Adamts13*$^{-/-}$ mice compared with age-matched WT, *Adamts13*$^{-/-}$, or *APPPS1* littermate mice (Fig 2E and 2F and S3A Fig), beginning at 2 months and peaking at 12 months. Double immunostaining of CD31^{+} endothelium and ZO-1 (S3B, S3C and S3D Fig.) or VE-cadherin (S3E and S3F Fig) confirmed significant age-dependent reductions in both junctional proteins in the cortex and hippocampus of *APPPS1–Adamts13*$^{-/-}$ mice. No significant changes in ZO-1 and VE-cadherin were observed in 2- and 6-month-old *APPPS1* mice. At 12 months, *APPPS1* mice also showed reductions in ZO-1 and VE-cadherin, but they were less marked than the reductions observed in *APPPS1–Adamts13*$^{-/-}$ mice. In addition, quantification of the coverage of pericyte on brain microvessels in the cortex (Fig 2G) and hippocampus (Fig 2H and S4 Fig) revealed no significant differences in 2-, 6-, and 12-month-old *Adamts13*$^{-/-}$ and *APPPS1* mice compared with age-matched WT littermates. Microvascular pericytes in the cortex and hippocampus were

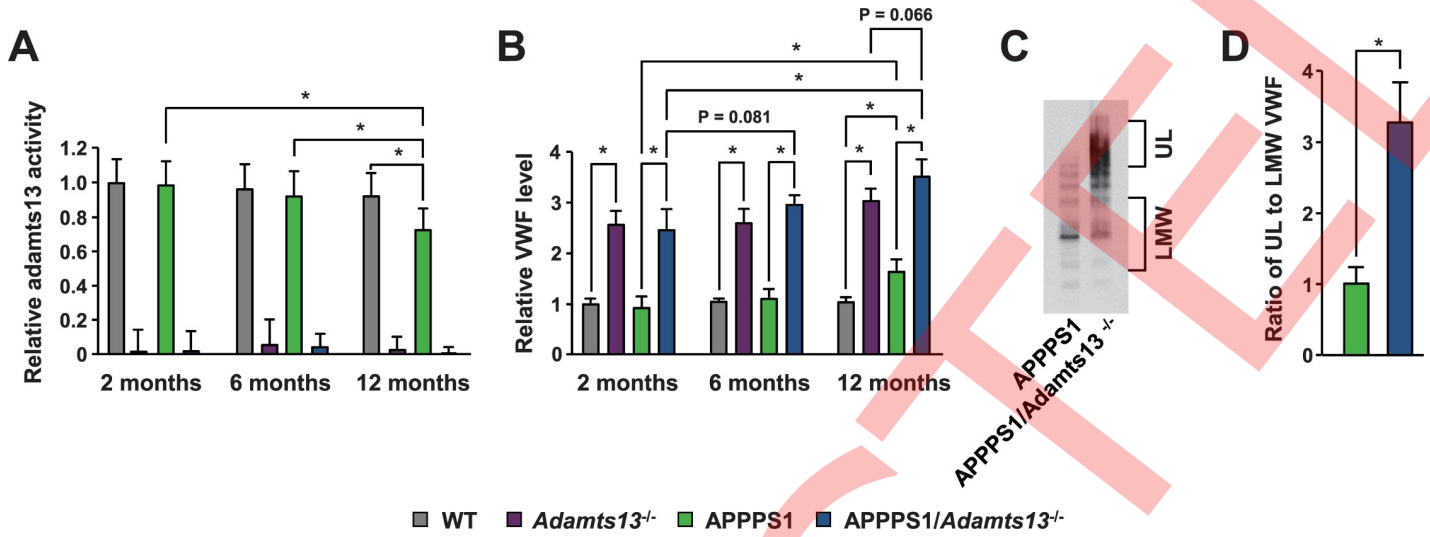

Fig 1. ADAMTS13 activities and VWF levels in murine plasma. (A) ADAMTS13 activities in plasma from 2-, 6-, and 12-month-old WT, *Adamts13*$^{-/-}$, *APPPS1*, and *APPPS1–Adamts13*$^{-/-}$ mice ($n = 6$). (B) VWF levels in plasma from 2-, 6-, and 12-month-old WT, *Adamts13*$^{-/-}$, *APPPS1*, and *APPPS1–Adamts13*$^{-/-}$ mice ($n = 6$). (C) Representative immunoblotting analysis of plasma VWF multimers from 12-month-old *APPPS1* and *APPPS1–Adamts13*$^{-/-}$ mice. (D) Quantitative analysis of the ratio of UL to LMW) VWF multimers in each group ($n = 5$). Relevant data values are included in S1 Data. Values are mean ± SD. $^{*}P < 0.05$. ADAMTS13, a disintegrin and metalloprotease with thrombospondin type I motif, member 13; APPPS1, amyloid precursor protein–presenilin 1; LMW, low molecular weight; UL, ultralarge; VWF, von Willebrand factor; WT, wild type.

https://doi.org/10.1371/journal.pbio.3000313.g001

significantly reduced in 6- and 12-month-old *APPPS1–Adamts13*$^{-/-}$ mice compared with those in age-matched WT, *Adamts13*$^{-/-}$, and *APPPS1* littermate mice.

ADAMTS13 deficiency leads to microvascular and cerebral blood flow reductions in *APPPS1* mice

To address whether the early BBB breakdown and loss of the BBB properties in *APPPS1–Adamts13*$^{-/-}$ mice were associated with microvascular degeneration, brain capillary density was analyzed by CD31 staining. We found greater than 36% to 39% and 29% to 38% reductions in capillary density in 6-month-old *APPPS1–Adamts13*$^{-/-}$ mice in the cortex and hippocampus, respectively, when compared with other genotypes (Fig 3A and 3C and S5A and S5B Fig). At 12 months, *APPPS1* mice displayed 31% and 36% reductions in cortical and hippocampal capillary density, respectively, when compared with WT littermates, as reported [28,29]. ADAMTS13 deficiency in *APPPS1* mice resulted in even greater than 25% and 41% reductions in cortical and hippocampal capillary density compared with *APPPS1* mice. There was no difference in capillary density among 2-month-old WT, *Adamts13*$^{-/-}$, *APPPS1*, and *APPPS1–Adamts13*$^{-/-}$ mice.

To test whether the reduced capillary density reflects a decrease in brain capillary perfusion, we assessed the cortical vasculature using in vivo multiphoton microscopy imaging of intravenously injected FITC-dextran (MW = 2,000,000 Da). This analysis revealed a significant capillary perfusion deficit with a 34% to 40% reduction in the length of perfused cortical capillaries in 6-month-old *APPPS1–Adamts13*$^{-/-}$ mice compared with WT, *Adamts13*$^{-/-}$, and *APPPS1* littermate mice (Fig 3B and 3D). Compared with WT littermate mice, 12-month-old *APPPS1* mice showed a 37% reduction in the length of perfused cortical capillaries, but this was less marked than the 59% reduction observed in age-matched *APPPS1–Adamts13*$^{-/-}$ mice. Dynamic susceptibility contrast perfusion MRI of intravenously injected contrast agent gadopentetate dimeglumine revealed a significantly greater 43% reduction in hippocampal blood

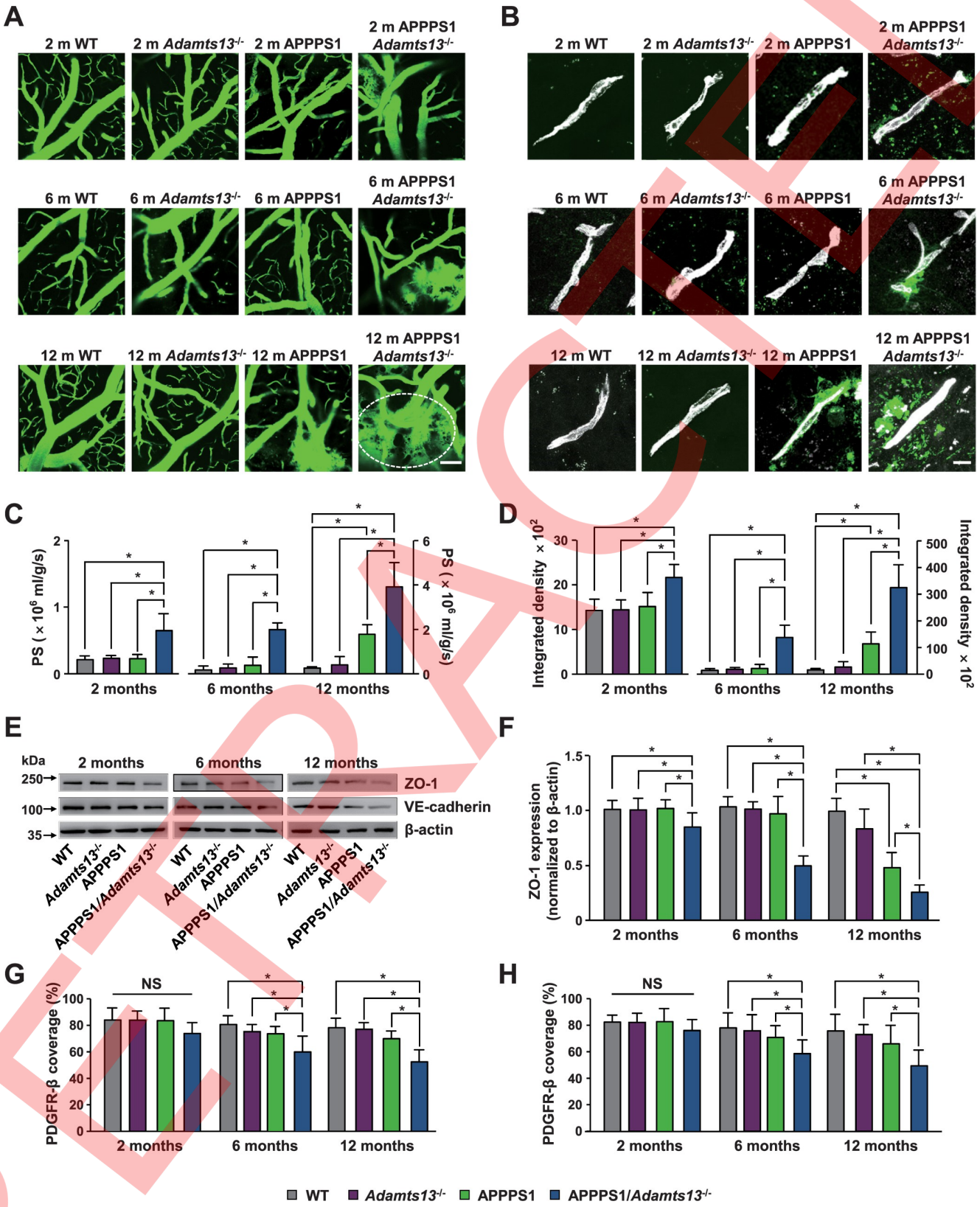

Fig 2. ADAMTS13 deficiency leads to early and progressive BBB breakdown in *APPPS1* mice. (A) In vivo multiphoton microscopy images of intravenously injected FITC-dextran (MW = 40,000 Da; green) leakage in cortical vessels in 2-, 6-, and 12-month-old WT, *Adamts13*$^{-/-}$, *APPPS1*, and

APPPS1–Adamts13$^{-/-}$ mice. Scale bar, 100 μm. (B) Representative images of fibrin extravascular deposits (green) and CD31^{+} microvessels (white) in the hippocampus of 2-, 6-, and 12-month-old WT, *Adamts13*$^{-/-}$, *APPPS1*, and *APPPS1–Adamts13*$^{-/-}$ mice. Scale bar, 10 μm. (C) Quantification of the PS product of FITC-dextran in WT, *Adamts13*$^{-/-}$, *APPPS1*, and *APPPS1–Adamts13*$^{-/-}$ mice ($n = 6$). Relevant data values are included in S1 Data. (D) Quantification of fibrin extravascular deposits in the hippocampus of WT, *Adamts13*$^{-/-}$, *APPPS1*, and *APPPS1–Adamts13*$^{-/-}$ mice ($n = 6$). (E) Representative immunoblots of the tight junction protein ZO-1 and the adherens junction protein VE-cadherin in isolated brain microvessels of WT, *Adamts13*$^{-/-}$, *APPPS1*, and *APPPS1–Adamts13*$^{-/-}$ mice. (F) Immunoblot analysis of the tight junction protein ZO-1 in isolated brain microvessels of WT, *Adamts13*$^{-/-}$, *APPPS1*, and *APPPS1–Adamts13*$^{-/-}$ mice ($n = 6$). Relevant data values are included in S1 Data. (G–H) Quantification of PDGFR-β^{+} pericyte coverage on CD31^{+} microvessels in the cortex (G) and hippocampus (H) in WT, *Adamts13*$^{-/-}$, *APPPS1*, and *APPPS1–Adamts13*$^{-/-}$ mice ($n = 6$). Relevant data values are included in S1 Data. Values are mean ± SD. $^{*}P < 0.05$. ADAMTS13, a disintegrin and metalloprotease with thrombospondin type I motif, member 13; APPPS1, amyloid precursor protein–presenilin 1; BBB, Blood-brain barrier; CD31, platelet endothelial cell adhesion molecule-1; FITC, fluorescein isothiocyanate; MW, molecular weight; NS, not significant; PDGFR-β, plate-derived growth factor receptor-β; PS, permeability surface; VE, vascular endothelial-cadherin; WT, wild type; ZO-1, Zonula Occludens-1. The 12m APPPS1 panel of Figure 2A is excluded from this article's CC-BY license. See the accompanying retraction notice for more information.

https://doi.org/10.1371/journal.pbio.3000313.g002

flow in 12-month-old *APPPS1–Adamts13*$^{-/-}$ mice compared with WT littermates that was more potent than the 24% reduction found in *APPPS1* mice (Fig 3E and 3F). These data are consistent with previous reports showing that regional brain capillary density correlates with blood flow [30,31].

ADAMTS13 deficiency accelerates AD pathology and impairs cognitive function in *APPPS1* mice

Next, we examined whether ADAMTS13 deficiency causing brain vascular damage and regional cerebral blood flow reduction can influence Aβ pathology in *APPPS1* mice. At 12 months of age, soluble and insoluble Aβ40 and Aβ42 were increased by 62%, 52%, 62%, and 36% in brains of *APPPS1–Adamts13*$^{-/-}$ mice, respectively, compared with those in *APPPS1* littermates (Fig 4A and 4B). Aβ immunostaining and thioflavin S (ThS) staining confirmed this observation, showing that the cortical and hippocampal plaque load were markedly elevated in *APPPS1–Adamts13*$^{-/-}$ mice compared with *APPPS1* mice (Fig 4C, 4D and 4E). Furthermore, *APPPS1–Adamts13*$^{-/-}$ mice developed 2.3-fold and 1.7-fold increases in cerebral amyloid angiopathy (CAA) and parenchymal amyloid deposition, respectively, as measured by in vivo multiphoton imaging of methoxy-X04^{+} amyloid plaques and Tetramethylrhodamine (TMR)-dextran angiopathy (Fig 4F and 4G). Notably, the CAA load was positively correlated with the BBB permeability determined by the permeability surface (PS) product for FITC-dextran in *APPPS1* and *APPPS1–Adamts13*$^{-/-}$ mice (Fig 4H).

To determine whether ADAMTS13 deficiency in *APPPS1* mice affected Aβ production and APP processing, we examined APP metabolism. Consistent with previous reports [32,33], significant increases in the levels of full-length APP and β-secretase (BACE1) and APP C-terminal fragments (β-CTFs and α-CTFs) were observed in brain homogenates from 12-month-old *APPPS1* mice compared with age-matched WT controls (Fig 4I and S6 Fig). However, the levels of these proteins were similar in *APPPS1* and *APPPS1–Adamts13*$^{-/-}$ mice, suggesting that accelerated Aβ brain accumulation and CAA observed in *APPPS1–Adamts13*$^{-/-}$ mice did not result from increased Aβ production and processing. Another key mechanism underlying increased Aβ brain accumulation is reduced clearance of Aβ from the brain [2,19,34]. Therefore, we tested whether the expression of the Aβ BBB-transporting proteins is altered in *APPPS1–Adamts13*$^{-/-}$ mice. Western blot analysis of Aβ efflux transporters in isolated brain capillaries revealed significant down-regulation of low-density lipoprotein receptor-related protein 1 (LRP1) and P-glycoprotein (P-gp) in *APPPS1* mice compared with WT mice (Fig 4I and 4J), consistent with earlier reports [35–37]. We then found a marked decrease in LRP1 and P-gp in *APPPS1–Adamts13*$^{-/-}$ mice compared with *APPPS1* mice. The level of the Aβ influx transporter receptor for advanced glycation end products (RAGE) did not change

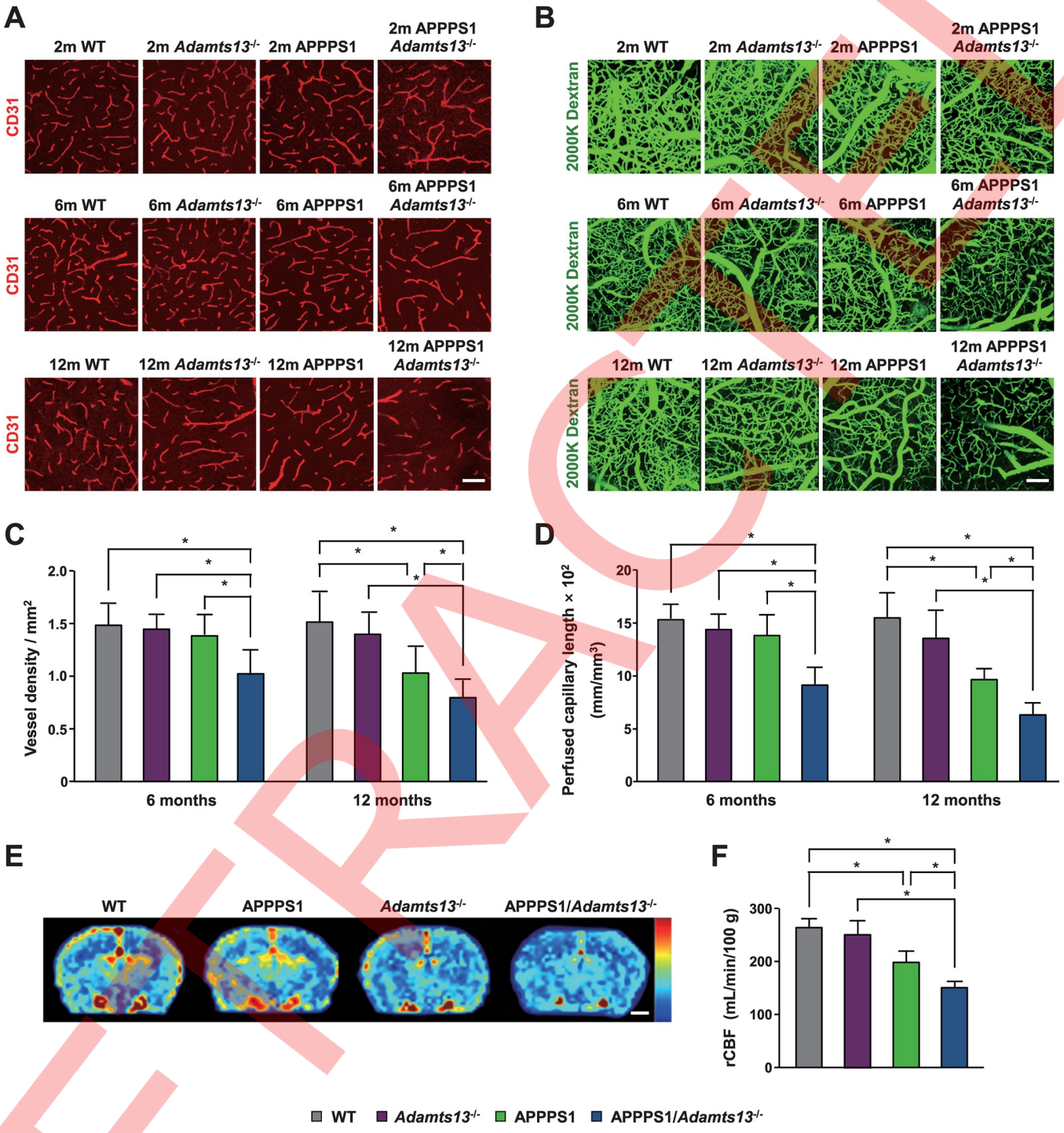

Fig 3. ADAMTS13 deficiency leads to microvascular and cerebral blood flow reductions in *APPPS1* mice. (A) Confocal images of CD31^{+} microvessels in the cortex of 2-, 6-, and 12-month-old WT, *Adamts13*$^{-/-}$, *APPPS1*, and *APPPS1–Adamts13*$^{-/-}$ mice. Scale bar, 50 μm. (B) In vivo multiphoton microscopy images of perfused cortical capillaries with intravenously injected FITC-dextran (MW = 2,000,000 Da). (C–D) Quantification of microvascular density (C) and perfused capillary length (D) in 6- and 12-month-old WT, *Adamts13*$^{-/-}$, *APPPS1*, and *APPPS1–Adamts13*$^{-/-}$ mice ($n = 6$). Relevant data values are included in S1 Data. (E–F) Representative rCBF maps generated from dynamic susceptibility contrast perfusion MRI (E) and quantification of rCBF at the hippocampal levels (F) in 12-month-old WT, *Adamts13*$^{-/-}$, *APPPS1*, and *APPPS1–Adamts13*$^{-/-}$ mice ($n = 5$). Scale bar, 1 mm. Relevant data values are included in S1 Data. Values are mean ± SD. $^{*}P < 0.05$. ADAMTS13, a disintegrin and metalloprotease with thrombospondin type I motif, member 13; APPPS1, amyloid precursor protein–presenilin 1; CD31, platelet endothelial cell adhesion molecule-1; FITC, fluorescein isothiocyanate; MW, molecular weight; rCBF, relative cerebral blood flow; WT, wild type. The 6m WT panel of Figure 3B is excluded from this article's CC-BY license. See the accompanying retraction notice for more information.

https://doi.org/10.1371/journal.pbio.3000313.g003

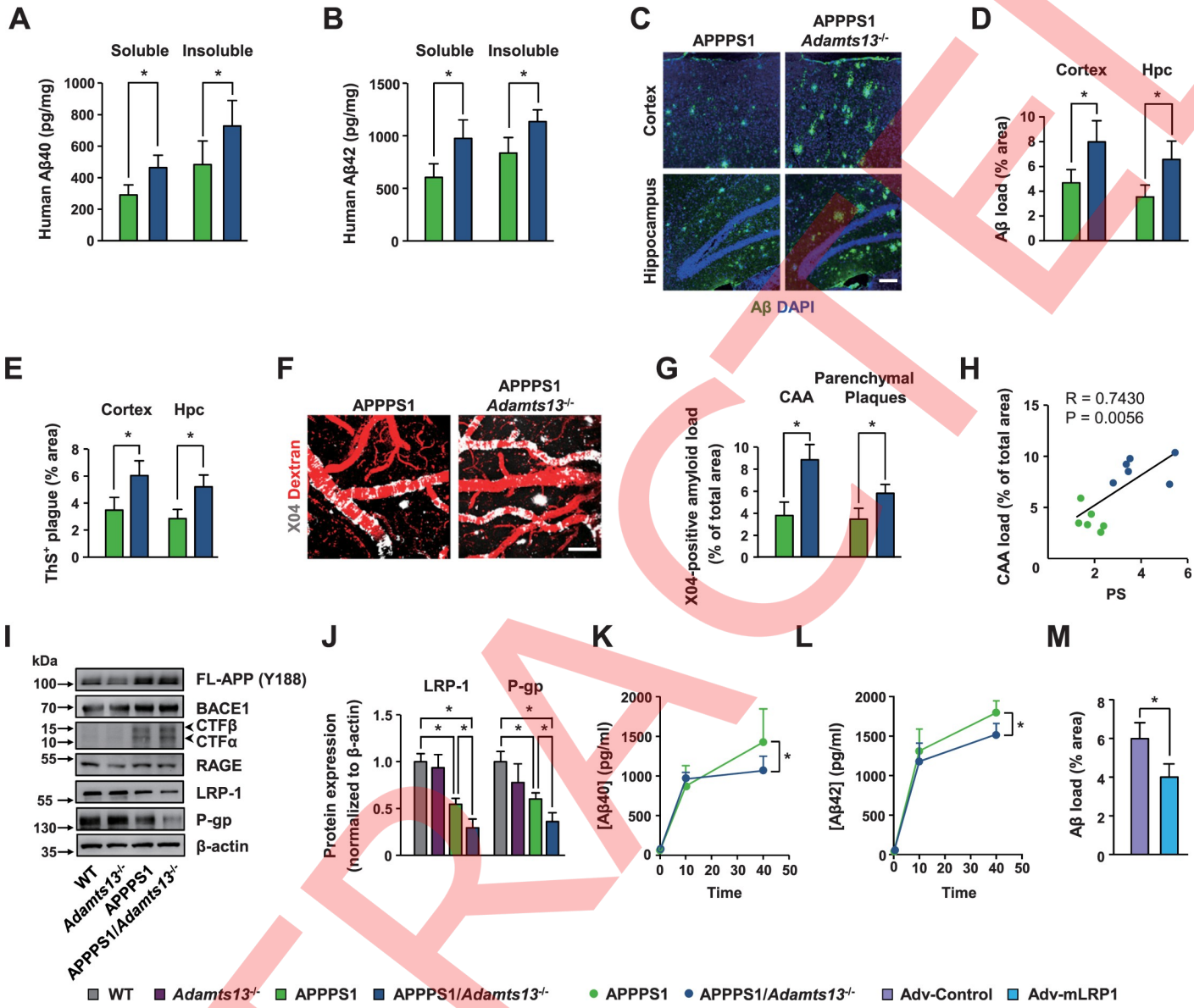

Fig 4. Accelerated AD pathology and impaired brain Aβ clearance in ADAMTS13-deficient *APPPS1* mice. (A–B) Amount of soluble and insoluble Aβ40 (A) and Aβ42 (B) in 12-month-old *APPPS1* and *APPPS1–Adamts13*$^{-/-}$ mice ($n = 6$). Relevant data values are included in S1 Data. (C) Representative micrographs of amyloid plaques labeled with antibody against Aβ from the cortex and hippocampus of 12-month-old *APPPS1* and *APPPS1–Adamts13*$^{-/-}$ mice. Scale bar, 100 μm. (D–E) Quantification of Aβ load (D) and ThS^{+} plaques (E) ($n = 6$). Relevant data values are included in S1 Data. (F–G) In vivo multiphoton microscopy images of methoxy-X04 labeled Aβ plaques (white) and cerebral angiopathy with TMR-dextran (red) (F) and quantification of CAA load and parenchymal X04^{+} amyloid load (G) in the cortex of *APPPS1* and *APPPS1–Adamts13*$^{-/-}$ mice ($n = 6$). Scale bar, 100 μm. Relevant data values are included in S1 Data. (H) Linear relationship between the CAA load and the BBB permeability determined by the PS product for FITC-dextran in *APPPS1* and *APPPS1–Adamts13*$^{-/-}$ mice. Relevant data values are included in S1 Data. (I) Immunoblot analysis of full-length APP, CTFs, and BACE1 in brain tissue and Aβ BBB-transporting proteins RAGE, LRP1, and P-gp in isolated brain microvessels of WT, *Adamts13*$^{-/-}$, *APPPS1*, and *APPPS1–Adamts13*$^{-/-}$ mice. (J) Quantification of LRP1 and P-gp ($n = 5$). Relevant data values are included in S1 Data. (K–L) Plasma accumulation of brain-derived Aβ40 (panel K) and Aβ42 (panel L) before, 10 minutes after, and 40 minutes after the Aβ stabilizing anti-Aβ antibody HJ5.1 injection ($n = 6$). Relevant data values are included in S1 Data. (M) Quantification of Aβ load in the hippocampus of 12-month-old *APPPS1–Adamts13*$^{-/-}$ mice treated with Adv-Con and Adv-mLRP1 ($n = 5$). Relevant data values are included in S1 Data. Values are mean ± SD. $^{*}P < 0.05$. AD, Alzheimer disease; ADAMTS13, a disintegrin and metalloprotease with thrombospondin type I motif, member 13; Adv-Con, control adenovirus; Adv-mLRP1, adenovirus carrying an LRP1 minigene; APP, amyloid precursor protein; APPPS1, amyloid precursor protein–presenilin 1; Aβ, amyloid-β; BACE1, β-secretase; BBB, Blood-brain barrier; CAA, cerebral amyloid angiopathy; CTF, C-terminal fragment; FITC, fluorescein isothiocyanate; FL-APP, Full length APP; HJ5.1, Aβ-stabilizing anti-Aβ antibody HJ5.1; Hpc, hippocampus; LRP1, lipoprotein receptor-related protein 1; P-gp, P-glycoprotein; PS, permeability surface; r, Pearsonâ s coefficient; RAGE, receptor for advanced glycation end products; ThS, thioflavin S; TMR, Tetramethylrhodamine; WT, wild type.

https://doi.org/10.1371/journal.pbio.3000313.g004

(S6 Fig). Using established protocols [38, 39], we next examined the brain Aβ elimination into the blood of mice using an Aβ-stabilizing anti-Aβ antibody HJ5.1 (HJ5.1) that binds brain-derived Aβ within the blood to prevent its rapid degradation. This analysis showed a significant reduction in the plasma levels of Aβ40 and Aβ42 at 40 minutes after injection of HJ5.1 in *APPPS1–Adamts13*$^{-/-}$ mice compared with *APPPS1* mice (Fig 4K and 4L), indicating that ADAMTS13 deficiency impeded Aβ clearance from the brain into blood. Finally, we tested whether overexpression of LRP1 in brain microvessels in *APPPS1–Adamts13*$^{-/-}$ mice affects Aβ pathology. Consistent with findings that LRP1 is a key Aβ clearance protein [31], adenoviral-mediated overexpression of a human LRP1 minigene in the hippocampus of *APPPS1–Adamts13*$^{-/-}$ mice (S7A Fig) resulted in a significant reduction in Aβ load (Fig 4M and S7B Fig).

To assess the functional outcome of ADAMTS13 deficiency in *APPPS1* mice, we first examined spatial learning and memory using the Morris water maze (MWM) test. At 12 months, *APPPS1* mice had significant impairments of learning and memory (Fig 5A, 5B and 5C), consistent with earlier reports [40,41]. Compared with *APPPS1* mice, *APPPS1–Adamts13*$^{-/-}$ mice showed significantly worse performance, as indicated by a significant increase in the escape latency time during the hidden platform test (Fig 5A), fewer platform crossings (Fig 5B), and shorter time spent in the platform quadrants (Fig 5C) during the probe trials. We next used the Y-maze test. *APPPS1–Adamts13*$^{-/-}$ mice exhibited a significantly lower rate of spontaneous alternations than other genotypes (Fig 5D), indicating a more severe working memory deficit. We also performed the passive avoidance test to assess the cognitive functions of animals [42]. This analysis showed that all mice exhibited comparable initial latencies to enter the dark compartment (Fig 5E). Compared with other groups, *APPPS1–Adamts13*$^{-/-}$ mice took a shorter time to reenter the dark compartment during the retention session, showing an impairment of memory. In addition, animals were tested in the open-field test. We found a significantly lower number of rearings (Fig 5F) and a shorter traveling distance (S8 Fig) in *APPPS1–Adamts13*$^{-/-}$ mice compared with other genotypes. These data indicate that *APPPS1–Adamts13*$^{-/-}$ mice had worse locomotor activity than the control *APPPS1* mice. To examine whether early cerebrovascular changes in *APPPS1–Adamts13*$^{-/-}$ mice are associated with cognitive decline, the Y-maze test was performed in 5-month-old mice. Consistent with previous reports [43–45], *APPPS1* mice exhibited a significant impairment in working memory (Fig 5G). ADAMTS13 deficiency caused further worsening of performance in *APPPS1* mice.

Reduced dendritic spines have been implicated in cognitive impairment of AD [46,47]. We next examined whether impaired vascular functions by ADAMTS13 deficiency could induce synaptic dysfunction. Golgi staining revealed a 24% reduction in dendritic length (Fig 5H, 5I and 5J) and a 30% loss of spine density (Fig 5K) in the field CA1 of hippocampus (CA1) of *APPPS1* mice at 12 months compared with age-matched WT littermates as well as a more severe 46% reduction in dendritic length and a 43% loss of spine density in *APPPS1–Adamts13*$^{-/-}$ mice compared with age-matched WT littermates. In contrast, 2-month-old *APPPS1–Adamts13*$^{-/-}$ mice did not show evidence of Aβ deposition and synaptic loss (S9A, S9D and S9E Fig). The levels of soluble Aβ40 and Aβ42 in brains of 2-month-old *APPPS1–Adamts13*$^{-/-}$ were comparable to that of age-matched *APPPS1* mice (S9B and S9C Fig). To further determine whether ADAMTS13 deficiency may affect the synaptic function, we performed whole-cell patch clamp recordings on hippocampal CA1 neurons in brain slices from 2-month-old mice. There were no significant changes in miniature excitatory postsynaptic current (mEPSC) frequency and amplitude among WT, *Adamts13*$^{-/-}$, *APPPS1*, and *APPPS1–Adamts13*$^{-/-}$ mice (S9F, S9G and S9H Fig). However, BBB breakdown and loss of endothelial junctions in *APPPS1–Adamts13*$^{-/-}$ mice were already detectable at this age (Fig 2A, 2B, 2C, 2D, 2E and 2F and S2A, S2B, S2C, S3A, S3B, S3C, S3D, S3E and S3F Figs). These data indicate

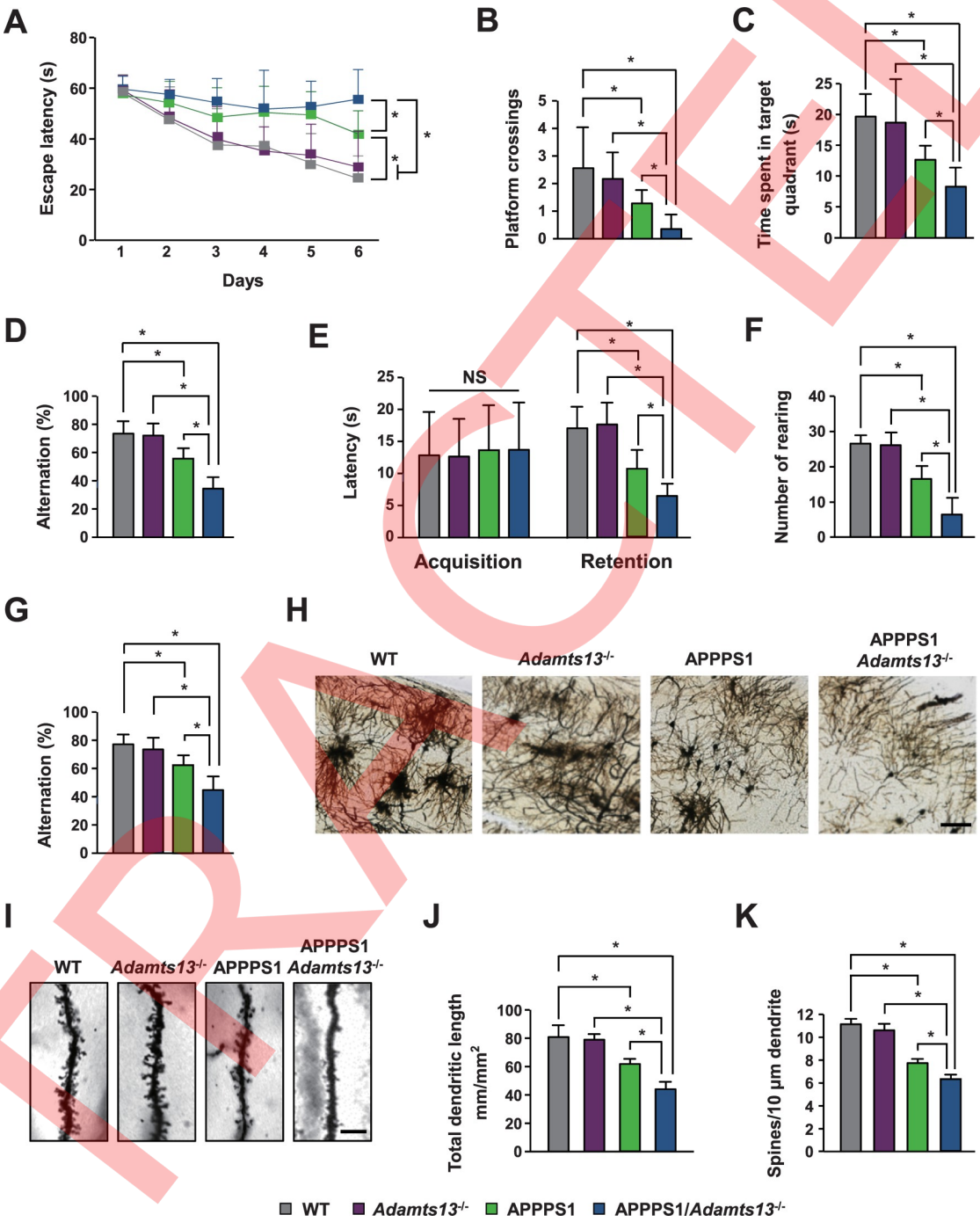

Fig 5. ADAMTS13 deficiency accelerates cognitive impairment and synaptic loss in *APPPS1* mice. (A–F) WT, *Adamts13*$^{-/-}$, *APPPS1*, and *APPPS1–Adamts13*$^{-/-}$ mice (n = 12–15 mice at 12 months) were subjected to the MWM, Y-maze, passive avoidance, and open-field test. Escape latency during platform trials (A), number of platform crossings (B), and time spent in the target quadrant in probe trial (C) of the MWM test. (D) Alternation of arms in the spontaneous alternation test of the Y-maze test. (E) Latencies to enter the dark compartment in the passive avoidance test. (F) Number of rearing in open-field test. (G) Y-maze test in 5-month-old WT, *Adamts13*$^{-/-}$, *APPPS1*, and *APPPS1–Adamts13*$^{-/-}$ mice (n = 12). Relevant data values are included in S1 Data. (H–I) Representative images of dendritic length (H) and dendritic spines (I) in the hippocampal CA1 region of WT, *Adamts13*$^{-/-}$, *APPPS1*, and *APPPS1–Adamts13*$^{-/-}$ mice at 12 months. Scale bar, 100 μm (H) and 10 μm (I). (J–K) Quantification of total dendritic length (J) and spine number per 10 μm of dendrite (K) for each group (n = 3). Relevant data values are included in S1 Data. Values are mean ± SD. $^{*}P < 0.05$. ADAMTS13, a disintegrin and metalloprotease with thrombospondin type I motif, member 13; APPPS1, amyloid precursor protein–presenilin 1; CA1, field CA1 of hippocampus; MWM, Morris Water Maze; NS, not significant; WT, wild type.

https://doi.org/10.1371/journal.pbio.3000313.g005

that vascular damage precedes the development of plaque load and synaptic dysfunction in the brain of *APPPS1–Adamts13*$^{-/-}$ mice.

Virus-mediated expression of ADAMTS13 reverses BBB breakdown and microvascular and cerebral blood flow reductions in *APPPS1* mice

Next, we studied the role of ADAMTS13 in *APPPS1* mice by injecting recombinant adeno-associated virus serotype 8 (AAV8)-mediated expression of a murine ADAMTS13 variant (AAV8-ADAMTS13) into the hippocampi of 9-month-old *APPPS1* mice, which already exhibited vascular damage, plaque deposition, and cognitive deficits [25,48,49]. After 3 months of virus injection, the mice were tested at 12 months of age. Confocal microscopy analysis for red fluorescent protein (RFP) indicated that the cortex and hippocampus were extensively transduced at 3 months after injection (Fig 6A). Expression of the truncated ADAMTS13 variant in the cortex and hippocampus was demonstrated by immunoblot analyses, using the antibody that recognizes the metalloproteinase domain of ADAMTS13 (Fig 6B). Multiphoton microscopy analysis of FITC-dextran indicated a substantial reduction in BBB permeability in *APPPS1* mice treated with AAV8-ADAMTS13 compared with control mice treated with AAV8-RFP (Fig 6C and 6D). No significant differences were observed in microvascular pericytes between control and AAV8-ADAMTS13 adenovirus groups (Fig 6E). Administration of AAV8-ADAMTS13 into *APPPS1* mice also caused a significant increase in the capillary density in the cortex and hippocampus and the length of perfused cortical microvessels (Fig 6F, 6G, 6H and 6I). Contrast perfusion MRI revealed that AAV8-ADAMTS13 treatment restored hippocampal blood flow in *APPPS1* mice (Fig 6J and 6K).

Virus-mediated expression of ADAMTS13 reduces Aβ deposition to improve cognitive deficits of *APPPS1* mice

We asked whether the improved vascular function and regional cerebral blood flow by AAV8-ADAMTS13 could improve AD pathology. At 12 months, *APPPS1* mice that received AAV8-ADAMTS13 exhibited reduced levels of brain-soluble and -insoluble Aβ40 and Aβ42 relative to AAV8-RFP–treated controls (Fig 7A and 7B). The cerebral Aβ plaque load was markedly reduced by 41% and 46% in the cortex and hippocampus, respectively, in *APPPS1* mice subjected to AAV8-ADAMTS13 injection (Fig 7C and S10A Fig). Plaque staining with ThS confirmed the reduced amyloid plaques in mice injected with AAV8-ADAMTS13 (Fig 7D and S10B Fig). Furthermore, the profiles of CAA and parenchymal amyloid deposition in mice injected with AAV8-ADAMTS13 were significantly reduced compared with those of the control mice (Fig 7E and 7F). Western blot analysis of isolated brain capillaries revealed that AAV8-ADAMTS13 injection led to significantly higher levels of Aβ BBB-transporting proteins LRP1 and P-gp than did AAV8-RFP injection (Fig 7G and 7H). In line with these data, we found significantly increased Aβ elimination from brain to blood in mice injected with AAV8-ADAMTS13 (Fig 7I and 7J). Collectively, these results suggest that the ADAMTS13 expression by virus administration likely decreased Aβ accumulation in the brains of *APPPS1* mice via increased BBB-mediated Aβ clearance.

We next determine the roles of ADAMTS13 in Aβ uptake and degradation in human cerebral microvascular endothelial (hCMEC/D3) cells. Aβ uptake was assessed by the addition of Aβ1–42 labeled with 5(6)-carboxyfluorescein (FAM-Aβ42) to the media of hCMEC/D3 cells in the presence and absence of human recombinant ADAMTS13 (rADAMTS13). This analysis showed that the levels of intracellular Aβ42 was enhanced in a time-dependent manner (Fig 7K). Treatment with rADAMTS13 significantly increased Aβ42 uptake following 30, 45, and 60 minutes of FAM-Aβ42 incubation compared with vehicle-treated hCMEC/D3 cells. To

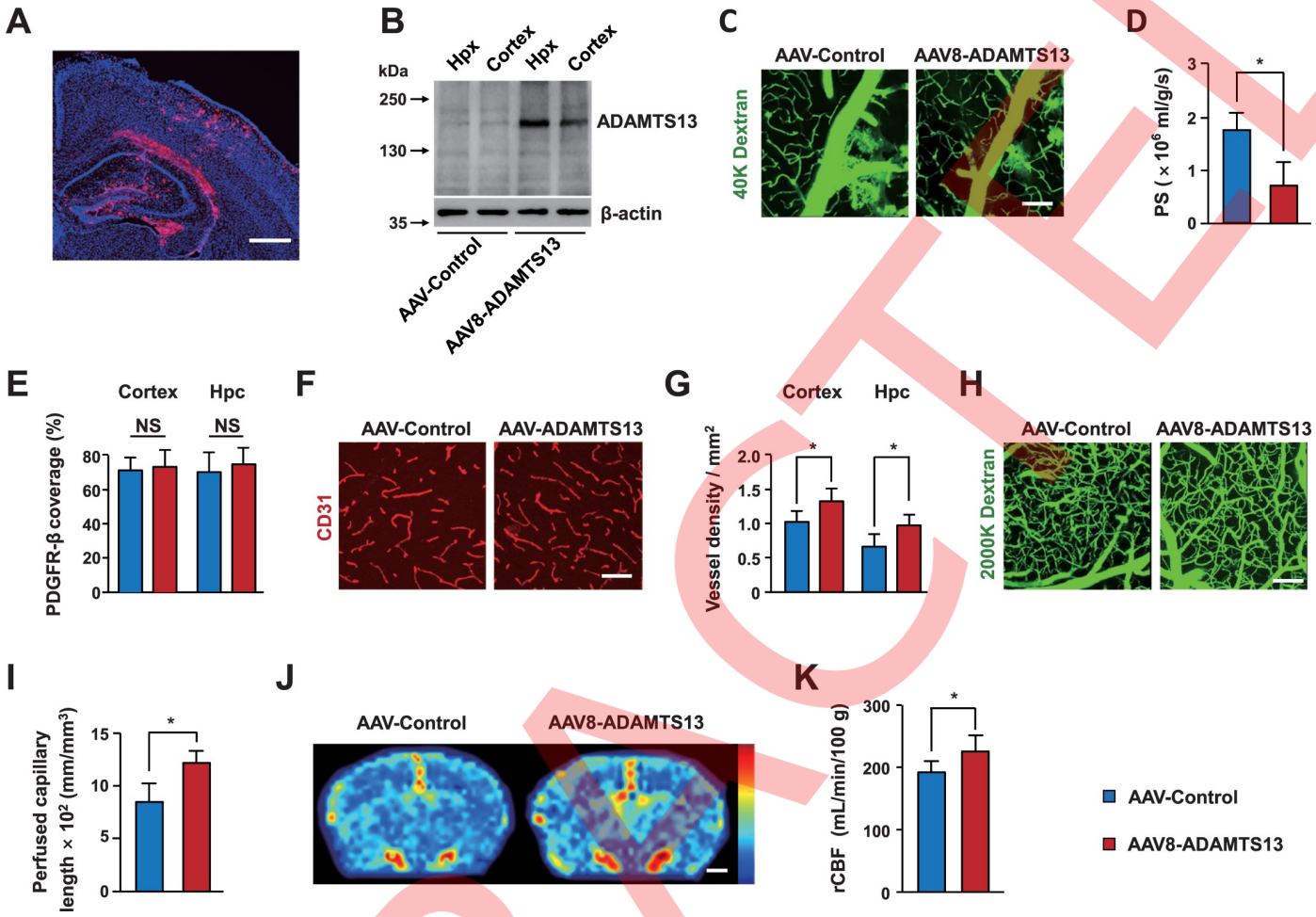

Fig 6. ADAMTS13 adeno-associated virus treatment reduces vascular dysfunction in *APPPS1* mice. (A) Confocal images of the fluorescent signals in the brain of a 12-month-old mouse receiving AAV8-CMV-ADAMTS13 injection. Scale bar, 200 μm. (B) Immunoblotting analysis of transduced ADAMTS13 variant in the Hpc and cortex of mice treated with AAV8-CMV-ADAMTS13 or AAV8 control. (C–D) In vivo multiphoton microscopy images of FITC-dextran (MW = 40,000 Da; green) leakage in cortical vessels (C) and quantification of the PS product of FITC-dextran (D) in 12-month-old *APPPS1* mice treated with AAV8-ADAMTS13 or control ($n = 6$). Scale bar, 100 μm. Relevant data values are included in S1 Data. (E) Quantification of PDGFR-β^+ pericyte coverage on CD31$^+$ microvessels in the cortex and Hpc in 12-month-old *APPPS1* mice treated with AAV8-ADAMTS13 or control ($n = 6$). Relevant data values are included in S1 Data. (F–G) Confocal images of CD31$^+$ microvessels in the cortex (F) and quantification of microvascular density in the cortex and Hpc (G) of 12-month-old *APPPS1* mice treated with AAV8-ADAMTS13 or control ($n = 6$). Relevant data values are included in S1 Data. (H–I) In vivo multiphoton microscopy images of perfused cortical capillaries with intravenously injected FITC-dextran (MW = 2,000,000 Da) (H) and quantification of perfused capillary length (I) in 12-month-old *APPPS1* mice treated with AAV8-ADAMTS13 or control ($n = 6$). Scale bar, 100 μm. Relevant data values are included in S1 Data. (J–K) Representative rCBF maps generated from dynamic susceptibility contrast perfusion MRI (J) and quantification of rCBF at the hippocampal levels (K) in 12-month-old *APPPS1* mice treated with AAV8-ADAMTS13 or control ($n = 5$). Scale bar, 1 mm. Relevant data values are included in S1 Data. Values are mean ± SD. $^*P < 0.05$. AAV8, adeno-associated virus serotype 8; ADAMTS13, a disintegrin and metalloprotease with thrombospondin type I motif, member 13; CD31, platelet endothelial cell adhesion molecule-1; CMV, cytomegalovirus; FITC, fluorescein isothiocyanate; Hpc, hippocampus; MW, molecular weight; NS, not significant; PDGFR-β, plate-derived growth factor receptor-β; PS, permeability surface; rCBF, relative cerebral blood flow. The AAV-Control panel of Figure 6C is excluded from this article's CC-BY license. See the accompanying retraction notice for more information.

https://doi.org/10.1371/journal.pbio.3000313.g006

quantify Aβ42 degradation, hCMEC/D3 cells were incubated with FAM-Aβ42 for 1 hour, followed by additional incubation for 2 hours without FAM-Aβ42. The levels of Aβ42 remaining were measured by ELISA and defined as degraded Aβ. We found that more Aβ42 was degraded by rADAMTS13-treated hCMEC/D3 cells (Fig 7L). Because astrocytes can take up and degrade Aβ [50], we also examined whether ADAMTS13 affects Aβ uptake and degradation in astrocytes. We observed a time-dependent increase in Aβ42 uptake in astrocytes (S11A Fig). However, Aβ42 uptake was not significantly change by rADAMTS13. ELISA analysis

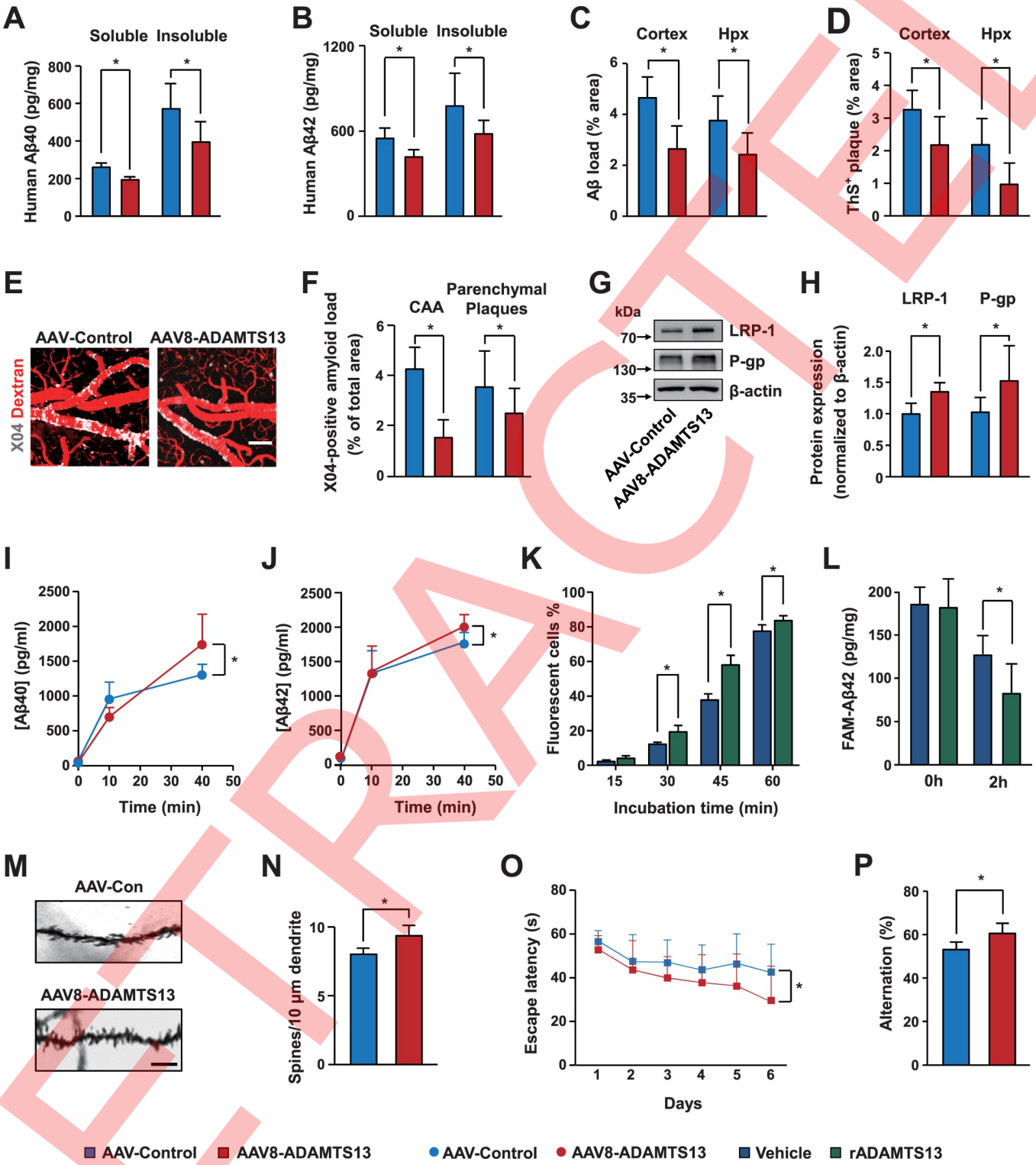

Fig 7. ADAMTS13 adeno-associated virus treatment reduces AD pathology and improves cognitive function in *APPPS1* mice. (A–C) Quantification of soluble and insoluble Aβ40 (panel A) and Aβ42 (panel B) and Aβ load (panel C) in 12-month-old *APPPS1* mice treated with AAV8-ADAMTS13 or control ($n = 6$). (D) Quantification of ThS^+ plaques in the cortex and Hpc ($n = 6$). (E–F) In vivo multiphoton microscopy images of methoxy-X04 labeled Aβ plaques (white) and cerebral angiopathy with TMR-dextran (red) (panel E) and quantification of CAA load and parenchymal $X04^+$ amyloid load (panel F) in the cortex of *APPPS1* mice treated with AAV8-ADAMTS13 or control ($n = 6$). Scale bar, 100 μm. (G–H) Immunoblots analysis (panel G) and quantification (panel H) of LRP1 and P-gp in isolated brain microvessels of *APPPS1* mice treated with AAV8-ADAMTS13 or control ($n = 5$). (I–J) Plasma accumulation of brain-derived

Aβ40 (panel I) and Aβ42 (panel J) before, 10 minutes after, and 40 minutes after the Aβ-stabilizing anti-Aβ antibody HJ5.1 injection in *APPPS1* mice treated with AAV8-ADAMTS13 or control ($n = 6$). (K) Internalization levels of Aβ42 were analyzed by flow cytometry in vehicle and rADAMTS13-treated hCMEC/D3 cells after incubation with FAM-Aβ42 for 15, 30, 45, and 60 minutes ($n = 5$). (L) hCMEC/D3 cells were incubated with FAM-Aβ42 for 1 hour, washed, and then incubated with FAM-Aβ42–free medium for 2 hours in the presence or absence of rADAMTS13. The residual Aβ42 was measured by ELISA ($n = 5$). (M–N) Representative images of Golgi-stained dendritic spines (panel M) and quantification of spine number per 10 μm of dendrite (panel N) in the hippocampal CA1 region of *APPPS1* mice treated with AAV8-ADAMTS13 or control. Scale bar, 10 μm ($n = 3$). (O) Escape latency during platform trials of the MWM test ($n = 13$–15). (P) Alternation of arms in the Y-maze test in 12-month-old APPPS1 treated with AAV8-ADAMTS13 or control viruses ($n = 13$–15). Relevant data values are included in S1 Data. Values are mean ± SD. $^{*}P < 0.05$. AAV8, adeno-associated virus serotype 8; AD, Alzheimer disease; ADAMTS13, a disintegrin and metalloprotease with thrombospondin type I motif, member 13; APPPS1, amyloid precursor protein–presenilin 1; Aβ, amyloid-β; CA1, field CA1 of hippocampus; CAA, cerebral amyloid angiopathy; ELISA, enzyme-linked immunosorbent assay; FAM-Aβ42, Aβ1–42 labeled with 5(6)-carboxyfluorescein; hCMEC/D3, human cerebral microvascular endothelial; HJ5.1, Aβ-stabilizing anti-Aβ antibody HJ5.1; Hpc, hippocampus; LRP1, lipoprotein receptor-related protein 1; MWM, Morris Water Maze; P-gp, P-glycoprotein; rADAMTS13, recombinant ADAMTS13; ThS, thioflavin S; TMR, Tetramethylrhodamine.

https://doi.org/10.1371/journal.pbio.3000313.g007

showed that rADAMTS13 also did not increase Aβ42 degradation in astrocytes (S11B Fig). Taken together, our results indicate that ADAMTS13 increased both the uptake and clearance of Aβ42 in cerebral microvascular endothelial cells but not in astrocytes. However, we cannot rule out the possibility that ADAMTS13 may also play a role in mediating Aβ clearance in other cell types.

The dendritic spine density in the hippocampal CA1 region was significantly increased in *APPPS1* mice injected with AAV8-ADAMTS13 (Fig 7M and 7N). We then tested whether the reversal of dendritic spine deficits in *APPPS1* mice could induce functional changes. In MWM tests, *APPPS1* mice injected with AAV8-ADAMTS13 took a shorter time to find the hidden platform in training sessions (Fig 7O), crossed the platform region more times (S12A Fig), and spent a longer time in the platform quadrants (S12B Fig) in the probe trials compared with AAV8-RFP–treated controls. In the Y-maze test, ADAMTS13 expression by virus administration reduced the percentage of spontaneous alternations (Fig 7P). In the open-field test, mice injected with AAV8-ADAMTS13 showed a significantly longer traveling distance (S12C Fig) and a higher number of rearings (S12D Fig) than AAV8-RFP–injected mice. Therefore, virus-mediated expression of ADAMTS13 in *APPPS1* mice effectively ameliorated behavioral deficits.

Discussion

In this study, we crossed the *APPPS1* mouse model of cerebral amyloidosis with *Adamts13*$^{-/-}$ mice and found that *APPPS1* mice lacking ADAMTS13 showed early and progressive BBB damage, capillary degeneration, and decreased blood flow. These cerebrovascular changes were associated with increased cerebral amyloid pathology and accelerated cognitive decline. In contrast, virus-mediated expression of ADAMTS13 in the brain of *APPPS1* mice reversed the vascular phenotype, AD-type pathologies, and behavioral deficits. Moreover, we demonstrated that the beneficial effect of ADAMTS13 appears to be due to increased Aβ clearance from brain to plasma as a consequence of improved BBB function.

There is increasing evidence that dysfunction of cerebral blood vessels is an early pathological event that occurs in dementia, including AD [19,51]. We found that ADAMTS13 deficiency induced BBB damage in the early disease stage in *APPPS1* mice, characterized by increased extravasation of administered FITC-dextran and serum fibrin and changes in endothelial junctions defined by loss of the tight junction protein ZO-1 and the adherens junction protein VE-cadherin. Consistent with previous reports that chronic BBB breakdown leads to microvascular dysfunction and elevated brain Aβ levels [52], we observed accelerated microvascular reductions, CAA formation, and Aβ deposition in elderly *APPPS1* mice lacking ADAMTS13. We further found reduced Aβ efflux transporters LRP1 and P-gp levels and Aβ brain-to-blood clearance in *APPPS1* mice lacking ADAMTS13. Aβ pathology was reversed in

the hippocampus of *APPPS1–Adamts13*$^{-/-}$ mice with adenoviral-mediated overexpression of LRP1. These results are consistent with previous reports demonstrating that LRP1-mediated Aβ clearance is critical for Aβ metabolism in the brain [1,31,53,54]. These findings also suggest that reduced vascular clearance of Aβ may contribute to the mechanisms by which ADAMTS13 deletion increased CAA formation and Aβ deposition. Moreover, the increased Aβ brain-to-blood clearance in AAV8-ADAMTS13–treated *APPPS1* mice was linked to reduced BBB defects. Together, our data suggest that ADAMTS13 may reduce CAA formation and Aβ accumulation by preserving BBB integrity and the associated improvement in cerebrovascular function and restoration of vascular responses.

Previous studies revealed that higher levels of VWF are seen in older adults and patients with vascular dementia [5,6,7]. However, the role of VWF and its cleaving protease ADAMTS13 in AD remains unknown. In this study, using an experimental model of AD, we have identified ADAMTS13 as an important regulator of AD-like pathology and cognitive decline. We also showed a significant increase in plasma VWF levels and a concomitant decrease in ADAMTS13 activity in *APPPS1* mice at 12 months of age. Deficiency of ADAMTS13 in *APPPS1* mice resulted in even greater increase in plasma VWF levels and UL-VWF multimers. Recent reports have demonstrated that ADMATS13 deficiency resulted in increased vascular injury [9,21], whereas VWF deficiency was protective [17]. Hence, it is possible that the phenotype of Aβ-associated cerebrovascular dysfunction and cognitive impairments observed in *APPPS1–Adamts13*$^{-/-}$ mice was caused by the synergistic pathological effects between VWF and Aβ. However, whether levels of ADAMTS13 in AD patients are reduced and its pathophysiologic relevance warrant further investigation.

BBB dysfunction and hypoperfusion have been linked to many pathological conditions of the central nervous system, including multiple sclerosis, stroke, and AD [19,51,55]. Our findings show that ADAMTS13 deficiency caused early cerebrovascular damage, resulting in microvascular and cerebral blood flow reductions, which in turn diminished BBB-mediated Aβ clearance and thereby worsened behavioral deficits. Our data demonstrate that virus-mediated expression of ADAMTS13 in brains of *APPPS1* transgenic mice led to decreased vascular insults and Aβ accumulation and improvement of cognitive performance. We propose that approaches to restore vascular functions may provide therapeutic value for improving cognitive decline in AD patients.

Materials and methods

Ethics statement

All animal experiments were approved by the Animal Care and Use Committee of Institutes of Brain Science, Fudan University (approval number 20150119–011).

Animals

Adamts13$^{-/-}$ mice were purchased from the Jackson Laboratory. *APPPS1* transgenic mice, which express a chimeric mouse/human amyloid precursor protein (Mo/Hu APP 695swe) with the mutant human presenilin 1 (PS1-dE9), were purchased from the Model Animal Research Center of Nanjing University. All mice were maintained on a C57BL/6 background. Male hemizygous *APPPS1* mice were crossed to female hemizygous *Adamts13*$^{-/-}$ mice to generate *APPPS1*, *Adamts13*$^{-/-}$, and *APPPS1–Adamts13*$^{-/-}$ mice and littermate nontransgenic controls. Mice were kept on a 12-hour light/dark cycle and had ad libitum access to food and water.

In vivo multiphoton imaging

In vivo time-lapse multiphoton images were taken as we previously described [17]. Briefly, in the parietal bone, a 2-mm–diameter window was opened, and a sterile cover glass was placed above the brain. Image experiments were performed using a multiphoton laser-scanning microscope (FV1200MPE, Olympus, Japan). Cerebrovascular permeability was evaluated by time-lapse imaging taken every 180 seconds for 20 minutes after FITC-dextran (40,000 Da, Sigma-Aldrich; 0.1 ml of 10 mg/ml) injection. To analyze perfusion of cortical microvessels, 0.1 ml bolus of FITC-dextran (2,000,000 Da, Sigma-Aldrich; 10 mg/ml) was injected intravenously. Multiphoton *z*-stack images were obtained from 200 μm below the surface of the cortex to a depth of 500 μm.

To visualize amyloid plaques, methoxy-XO4 (Tocris Bioscience, Bristol, UK; 10 mg/kg) was injected intraperitoneally into mice. Twelve hours later, the mice were anesthetized and implanted with a cranial window, and amyloid imaging was performed [56]. TMR-conjugated dextran (70,000 Da; Invitrogen, MA; 0.1 ml of 10 mg/ml) was intravenously injected before imaging to provide a fluorescent angiogram. In vivo images (500 × 500 μm) were acquired using a 25× objective. Each image was traced using ImageJ software. The thresholded TMR-dextran and methoxy-XO4 images were superimposed in 2 different layers. The TMR-dextran$^+$ area was selected, and the mean value of the pixels of the methoxy-XO4 image was calculated within the TMR-dextran selection. CAA load was presented as a percentage of methoxy-XO4$^+$ area covering TMR-dextran$^+$ area. See details in S1 Text.

Measurements of cerebral blood flow using MRI

Mice were anesthetized with 1% to 1.5% isoflurane in air/O_2 (2:1). MRI experiments were performed on a 9.4 T/400 mm scanner (Agilent Technologies, Santa Clara, CA), using a quadrature conformal surface coil (7.5mm–12.5mm) [57]. A series of T2-weighted MR images were collected before and after intravenous injection of contrast agent gadopentetate dimeglumine (Shanghai Xudong Haipu Pharmaceutical Co., Shanghai, China, 0.42 mmol/kg) via tail vein. See details in S1 Text.

Injection of adeno-associated virus vectors

Recombinant AAV8 encoding a C-terminal truncated murine ADAMTS13 variant (aa 1–2400) (pAAV8-CMV-ADAMTS13-P2A-mCherry-3FLAG) under a cytomegalovirus (CMV) promoter and control adenovirus only expressing the RFP AAV (pAAV8-CMV-P2A-mCherry-3FLAG) were prepared by Obio Technology (Shanghai, China). Previous studies have documented the safety and long-term expression of this AAV8-mediated expression of ADAMTS13 variant in a murine model of thrombotic thrombocytopenic purpura [58]. ADAMTS13 and RFP AAV8 were stereotactically bilaterally injected into the hippocampus (5×10^{12} viral genomes/ml, 2 μl per hippocampus) of the mice at 9 months of age. The following coordinates were used: anteroposterior +2.0 mm, mediolateral ±1.5 mm, and dorsoventral −1.5 mm [59]. The adenovirus carrying a human LRP1 minigene (Adv-mLRP1) and empty adenovirus (Adv-Con) were prepared (Obio Technology, Shanghai, China) and injected into the hippocampus of *APPPS1–Adamts13*$^{-/-}$ mice at 12 months of age, as described by Winkler and colleagues [31]. Injection of Adv-mLRP1 effectively induced the expression of LRP1 minigene in the hippocampus of *APPPS1–Adamts13*$^{-/-}$ mice (S7A Fig).

MWM

Experiments were conducted by investigators blinded to genotypes or treatments of mice for all behavioral measurements. The MWM was used to test spatial learning and reference memory functions [59]. See details in S1 Text.

Y-maze test

Y-maze tests are used to assess short-term spatial working memory [60]. The Y-maze consists of 3 black horizontal arms (36 cm long, 5 cm wide, and 10 cm high) at 120˚ angles to each other. See details in S1 Text.

Passive avoidance test

The passive avoidance test was assessed in a step-through box apparatus (Med Associates, St Albans, VT) consisting of a light compartment and a dark compartment [42]. The floor of each compartment contained a grid, with only the dark one being electrified by a generator. The mice were placed into the light compartment, and after 60 seconds, the guillotine door was opened. The latency to enter the dark compartment was recorded. Once entering the dark compartment, the mice received an immediate electrical shock (0.5 mA for 1 second). Mice were then returned to the home cages. After 24 hours, each mouse was again placed into the light compartment, and the latency to enter into the dark compartment was recorded for up to 300 seconds.

Open-field test

Mice were tested for 5 minutes in a clear 27.3 × 27.3 × 40 cm activity chamber (Med Associates, VT) with three 16-beam infrared arrays. See details in S1 Text.

Tissue preparation and ThS staining

Mice were deeply anesthetized; brains were removed and immersed with 4% paraformaldehyde in PBS at 4˚C. Frozen coronal sections of the brain were cut at 15-μm thickness with a cryostat (Leica Microsystems, IL) and stored at −80˚C until use. For ThS staining, brain sections were incubated in 1% ThS (T1892, Sigma-Aldrich, MO) for 10 minutes and rinsed in PBS. See details in S1 Text.

Immunohistochemistry

Frozen coronal brain sections were immunostained as described previously [17,61]. See details in S1 Text.

Analysis of extravascular fibrin deposition

Cerebral tissue cryosections were blocked with 5% normal donkey serum in PBS and incubated with a combination of antibodies of rat anti-CD31 (PECAM-1; 553370, 1:400; BD Pharmingen, NJ) and rabbit anti-fibrin (ogen) (AP00766PU-N, 1:2,000; Acris Antibodies, Germany) overnight at 4˚C. The sections were washed and incubated with Alexa Fluor 594 donkey anti-rat IgG and Alexa Fluor 488 donkey anti-rabbit IgG (Invitrogen, CA). To quantify extravascular deposits of fibrin, the images were contrast enhanced to clearly differentiate positivity from background and quantified using the NIH ImageJ integrated density analysis tool. For each animal, 6 fields from the cortex and 4 fields from the hippocampus in 6 sections (100 μm apart) were analyzed.

Preparation of brain microvessels and capillary-depleted brain homogenates

Mouse brain capillaries were isolated as previously described [17,30]. Briefly, brains were removed, and the meninges and large surface vessels were discarded. Brain tissue was

homogenized in ice-cold 16% dextran (Sigma-Aldrich, MO) in PBS containing 2% fetal bovine serum (FBS) with a glass dounce tissue grinder. Homogenates were centrifuged at 6,000*g* for 15 minutes at 4˚C. The supernatant was collected and centrifuged again to obtain capillary-depleted brain homogenates. Pellets were resuspended in PBS containing 1% BSA and passed through a 100-μm and 40-μm cell strainer (BD Falcon, San Jose, CA). Microvessels were collected from the 40-μm strainer membrane and used for experiments.

Western blotting

Brain tissues, brain capillaries, and capillary-depleted brain homogenates were lysed in RIPA lysis buffer (Millipore, MO) containing protease inhibitor cocktails (Roche Diagnostics, Basel, Switzerland). Equal amounts of protein were separated by SDS-PAGE electrophoresis, blotted onto a nitrocellulose membrane, and incubated with primary antibodies, followed by horseradish peroxidase-conjugated secondary antibodies (1:2,000; Cell Signaling Technology, MA). Signals were detected by an enhanced chemiluminescence detection reagent (PerkinElmer) and imaged using a ChemiDoc Touch imaging system with Quantity One software (Bio-Rad, Hercules, CA). See details in S1 Text.

ADAMTS13 activity assay

ADAMTS13 activity in plasma was determined using a commercial FRETS-VWF73 peptide (Peptides International, Louisville, KY) according to the manufacturerâ s instructions. Briefly, FRETS-VWF73 (100 μl of 4 mM, final concentration 2 μM) was incubated with 4 μl plasma in reaction buffer (5 mM Bis-Tris, 25 mM CaCl2, 0.005% Tween-20 [pH 6.0]). Fluorescence intensities were detected with a fluorescence spectrophotometer (Bio-Tech, Winooski, VT) every 5 minutes for 1 hour using excitation at 340 nm and emission at 450 nm.

Assay of VWF levels

VWF levels in plasma was measured as described by Zhu and colleagues [62]. Briefly, microtiter plates were coated with rabbit anti-VWF antibody (A0082, DAKO, CA) overnight at 4˚C. Plasma samples (1:40 diluted with 3% BSA in PBS) were incubated in the wells for 2 hours at room temperature. Then, the plates were incubated with 100 μl HRP-conjugated VWF (P0226, 1:2,000; DAKO, CA) for 1 hour at room temperature. After washing, 100 μl tetramethylbenzidine substrate (Sigma-Aldrich) was added to the wells. After 15 minutes, the reaction was stopped with 50 μl 2N HCL. Absorbance was read at 450 nm in an ELISA reader (Bio-Rad, CA). We could not achieve satisfactory analyses for ADAMTS13 activity and VWF levels in mice brains with commercially available antibodies, and thus these analyses were precluded from the study.

Assay of VWF multimers

The VWF multimers analysis was performed as described by Xu and colleagues [17]. Citrated plasma was diluted in sample buffer (70 mM Tris-HCl [pH 6.5], containing 2.4% sodium dodecyl sulfate, 4% urea, and 4 mM EDTA) and was incubated at 60˚C for 20 minutes. The sample was fractionated on a 1.2% SeaKem HGT agarose (50041, Rockland, ME) gel by electrophoresis and transferred onto nitrocellulose membrane (A10006746, Life Science, NJ). VWF multimers were visualized using a rabbit anti-VWF antibody (A0082, DAKO, CA). The signal was obtained using a ChemiDoc Touch imaging system (Bio-Rad, CA).

Aβ ELISA

Cortex and hippocampus were homogenized in ice-cold Tris buffer (50 mM Tris-HCl [pH 7.4], 150 mM NaCl, 50 mM EDTA, and 1% Triton X-100) with protease inhibitors (Roche Diagnostics, Basel, Switzerland) and centrifuged at 21,000*g* for 30 minutes at 4˚C. The supernatant was used for measurements of soluble Aβ fraction. For insoluble Aβ, the pellet was resuspended in 70% formic acid (10% v/w), homogenized, and ultracentrifuged at 100,000*g* for 60 minutes at 4˚C; formic acid-containing supernatants were neutralized with 1 M Tris buffer (pH 11). The levels of Aβ 40 and Aβ 42 in both fractions were quantified by Ultrasensitive Human ELISA Kits (KHB3482 and KHB3544, Invitrogen, MA) according to the instructions of the manufacturer.

Analysis of the elimination of brain Aβ into plasma

The efflux efficacy of brain-derived Aβ in blood was determined as described [38,39]. Briefly, an Aβ-stabilizing anti-Aβ antibody (HJ5.1, 150 μg/mouse; provided by Dr. David M. Holtzman, Washington University School of Medicine, St. Louis, MO) was injected intravenously into 12-month-old *APPPS1* transgenic mice. The anti-Aβ antibody HJ5.1 can rapidly bind brain-derived Aβ in the blood to prevent its degradation and allow direct measurement of the rate Aβ enters blood from the brain [38]. Blood was collected before, 10 minutes after, and 40 minutes after HJ5.1 antibody injection by retro-orbital bleeding. Plasma levels of Aβ 40 and Aβ 42 were quantified by using Ultrasensitive Human ELISA Kits (KHB3482 and KHB3544, Invitrogen, MA).

Cell cultures

hCMEC/D3 was purchased from DSMZ (CVCL-U985, Braunschweig, Germany). Cells were grown in EBM-2 medium (Lonza, Walkersville, MD) and supplemented with 5% FBS (Gibco, Rockville, MD), 1% penicillin (Gibco, MA), 1% streptomycin (Gibco, MA), 1.4 μM hydrocortisone (Sigma-Aldrich, MO), 5 μg/ml ascorbic acid (Sigma-Aldrich, MO), and 10 mM HEPES (Gibco, MA). Cultures were maintained at 37˚C in a humidified 95% air and 5% CO_2, and the medium was changed every 2 to 3 days. Primary cultures of astrocytes were prepared using cortices of postnatal day 1 C57BL/6 mice as described by Zhao and colleagues [63]. Briefly, cortices were minced and incubated with 2.5% trypsin (Gibco, MA) at 37˚C for 15 minutes. Dissociated cells were suspended in astrocyte growth medium containing Dulbecco's Modified Eagle Media (DMEM) and Ham's F12 (1:1 v/v) (Gibco, MA) with 10% FBS. The cells were passed through a 100-μm mesh sieve (BD Biosciences, NJ) and plated on poly-D-lysine-coated 75-flask in DMEM/F12, supplemented with 10% FBS, penicillin (100 U/ml, Gibco, MA), and streptomycin (100 μg/ml, Gibco, MA). The culture medium was changed every 2 to 3 days. When confluent, the cells were shaken at 260 rpm for 18 hours, and the medium was aspirated to remove microglial cells. Astrocyte purity was routinely >95% as assessed by glial fibrillary acidic protein (GFAP) immunostaining.

Preparation of Aβ42 peptides

Aβ1–42 labeled with 5(6)-carboxyfluorescein (FAM-Aβ42, AnaSpec, Fermont, CA) were dissolved in 1 mM 1,1,1,3,3,3-hexafluoro-2-propanol (HFIP) and incubated at room temperature for 2 hours. After the HFIP solution was removed by vacuum centrifugation (RVC 2–25 CD plus, Christ, Osterode, Germany), the remaining Aβ peptide was dissolved in DMSO at 5 mM and sonicated for 10 minutes. The peptide solution was incubated at 37˚C for 24 hours and

then centrifuged at 14,000*g* for 10 minutes at 4˚C. The supernatant containing soluble oligomers was stored at 4˚C.

Aβ uptake assays

hCMEC/D3 cells or astrocytes were seeded in 6-well plates and grown to confluence. FAM-Aβ42 (100 nM) was added 2 hours after addition of rADAMTS13 (60 ng/ml, R&D Systems, LA). After incubation for 15, 30, 45, and 60 minutes (for hCMEC/D3 cells) or 30, 60, and 120 minutes (for astrocytes), cells were rinsed 3 times with cold PBS and enzymatically detached using trypsin (Gibco, MA). Cells were centrifuged and resuspended in PBS and then incubated with 0.2% trypan blue (Gibco, MA) in PBS and fixed with 4% paraformaldehyde. Uptake was measured for fluorescence on a BD LSR Fortessa (BD Biosciences, NJ), and data were analyzed with FlowJo 10.0.8 software (FlowJo, https://www.flowjo.com).

Aβ efflux assays

hCMEC/D3 cells or astrocytes were initially incubated with FAM-Aβ42 for 1 hour (for hCMEC/D3 cells [54]) or 2 hours (for astrocytes). The medium was then removed, and cells were washed with warmed medium. The cells were then incubated in FAM-Aβ42–free medium for 2 hours at 37˚C in the presence or absence of rADAMTS13 (60 ng/ml). After washing, RIPA lysis buffer (Millipore, MO) containing protease inhibitor cocktails (Roche Diagnostics, Basel, Switzerland) was added to each well. After centrifugation, protein concentration was determined with the BCA protein assay (Thermo Scientific, MA). FAM-Aβ42 were quantified by Ultrasensitive Human ELISA Kits (KHB3544, Invitrogen, MA) according to the instructions of the manufacturer.

Statistical analysis

All data are represented as mean ± SD. Statistical tests were performed using GraphPad Prism (GraphPad Software, https://www.graphpad.com). Two-group comparisons were evaluated using the unpaired two-tailed Student *t* test. Multiple comparisons were analyzed by one-way ANOVA followed by the Bonferroni multiple comparison test. A linear correlation between 2 variables was performed using Pearsonâ s correlation coefficients. Differences with $P < 0.05$ were considered significant.

Supporting information

S1 Fig. Characterization of *APPPS1* and *APPPS1–Adamts13*$^{-/-}$ mice. (A) Western blot analysis of brain homogenates from WT, *APPPS1*, and *APPPS1–Adamts13*$^{-/-}$ mice, using the human-Aβ–specific antibody 6E10. (B) Western blot analysis of brain homogenates from WT, *APPPS1*, and *APPPS1–Adamts13*$^{-/-}$ mice, using the antibody, which recognizes both human and mouse APP. (C) Western blot analysis of brain homogenates from WT, *APPPS1*, and *APPPS1–Adamts13*$^{-/-}$ mice, using the PS1 C-terminal loop domain antibody. Filled arrow shows the full-length human PS1. Open arrow shows the human PS1-derived CTFs. Arrowhead shows the mouse PS1-derived CTFs. (D) PCR of tail genomic DNA prepared from WT, *APPPS1*, and *APPPS1–Adamts13*$^{-/-}$ mice. A 290-bp band specific for the targeting vector is observed only in *APPPS1–Adamts13*$^{-/-}$ mice. A 361-bp specific for the WT allele is observed only in WT and *APPPS1* mice. (E) RT-PCR analysis of liver RNA prepared from WT, *APPPS1*, and *APPPS1–Adamts13*$^{-/-}$ mice. APP, amyloid precursor protein; Aβ, amyloid-β; CTF, C-terminal fragment; PS1, presenilin 1; RT-PCR, reverse transcription-Polymerase Chain Reaction;

WT, wild type.
(PDF)

S2 Fig. Increased extravascular deposits of fibrin in the brain of *APPPS1–Adamts13*$^{-/-}$ mice. (A) Quantification of fibrin extravascular deposits in the cortex of 2-, 6-, and 12-month-old WT, *Adamts13*$^{-/-}$, *APPPS1*, and *APPPS1–Adamts13*$^{-/-}$ mice ($n = 6$). (B and C) Representative immunoblots (B) and quantification of fibrin (C) in capillary-depleted brain tissue in 2-, 6-, and 12-month-old WT, *Adamts13*$^{-/-}$, *APPPS1*, and *APPPS1–Adamts13*$^{-/-}$ mice ($n = 5$). Relevant data values are included in S2 Data. Values are mean ± SD. $^{*}P < 0.05$. WT, wild type.
(PDF)

S3 Fig. Age-dependent loss of tight and adherens junctions in *APPPS1–Adamts13*$^{-/-}$ mice. (A) Immunoblot analysis of the adherens junction protein VE-cadherin in isolated brain microvessels of WT, *Adamts13*$^{-/-}$, *APPPS1*, and *APPPS1–Adamts13*$^{-/-}$ mice ($n = 6$). (B–D) Double immunostaining for ZO-1 and CD31^{+} microvessels (B) and quantification of ZO-1–immunostained microvessels in the cortex (C) and hippocampus (D) of WT, *Adamts13*$^{-/-}$, *APPPS1*, and *APPPS1–Adamts13*$^{-/-}$ mice ($n = 6$). Scale bar, 50 μm. (E and F) Quantification of VE-cadherin–immunostained microvessels in the cortex (E) and hippocampus (F) of WT, *Adamts13*$^{-/-}$, *APPPS1*, and *APPPS1–Adamts13*$^{-/-}$ mice ($n = 6$). Scale bar, 50 μm. Relevant data values are included in S2 Data. Values are mean ± SD. $^{*}P < 0.05$. CD31, platelet endothelial cell adhesion molecule-1; VE, vascular endothelial-cadherin; WT, wild type; ZO-1, Zonula Occludens-1.
(PDF)

S4 Fig. Representative images of PDGFR-β+ pericyte coverage on CD31+ microvessels in the hippocampus in 2-, 6-, and 12-month-old WT, *Adamts13*$^{-/-}$, *APPPS1*, and *APPPS1–Adamts13*$^{-/-}$ mice. CD31, platelet endothelial cell adhesion molecule-1; PDGFR-β, plate-derived growth factor receptor-β; WT, wild type.
(PDF)

S5 Fig. The effects of ADAMTS13 deficiency on brain capillary profiles in *APPPS1* mice. (A and B) Confocal images of CD31^{+} microvessels (A) and quantification of microvascular density (B) in the hippocampus of 6- and 12-month-old WT, Adamts13$^{-/-}$, *APPPS1*, and *APPPS1–Adamts13*$^{-/-}$ mice ($n = 6$). Scale bar, 50 μm. Relevant data values are included in S2 Data. Values are mean ± SD. $^{*}P < 0.05$. ADAMTS13, a disintegrin and metalloprotease with thrombospondin type I motif, member 13; CD31, platelet endothelial cell adhesion molecule-1; WT, wild type. The APPPS1 Adamts13$^{-/-}$ panel of Figure S5A is excluded from this article's CC-BY license. See the accompanying retraction notice for more information.
(PDF)

S6 Fig. ADAMTS13 deficiency does not affect Aβ processing and the microvascular levels of Aβ influx transporter RAGE. Immunoblot analysis of full-length APP, CTFs, and BACE1 in brain tissue and RAGE in isolated brain microvessels of WT, *Adamts13*$^{-/-}$, *APPPS1*, and *APPPS1–Adamts13*$^{-/-}$ mice ($n = 5$). Relevant data values are included in S2 Data. Values are mean ± SD. $^{*}P < 0.05$. ADAMTS13, a disintegrin and metalloprotease with thrombospondin type I motif, member 13; APP, amyloid precursor protein; Aβ, amyloid-β; BACE1, β-secretase; CTF, C-terminal fragment; NS, not significant; RAGE, receptor for advanced glycation end products; WT, wild type.
(PDF)

S7 Fig. Overexpression of LRP1 in the hippocampus of APPPS1–Adamts13–/– mice using Adv-mLRP1. (A) Representative immunoblotting analysis of LRP-555 and mLRP1 in the Hpc

of *APPPS1–Adamts13*$^{-/-}$ mice treated with Adv-Con and Adv-mLRP1. (B) Representative micrographs of amyloid plaques labeled with antibody against Aβ from the hippocampus of 12-month-old *APPPS1–Adamts13*$^{-/-}$ mice treated with Adv-Con and Adv-mLRP1. Scale bar, 100 μm. Adv-Con, control adenovirus; Adv-mLRP1, adenovirus carrying an LRP1 minigene; Aβ, amyloid-β; Hpc, hippocampus; LRP-555, lipoprotein receptor-related protein-555; mLRP1, LRP1 minigene.
(PDF)

S8 Fig. Total distance traveled in the open-field test in 12-month-old WT, *Adamts13*$^{-/-}$, *APPPS1*, and *APPPS1–Adamts13*$^{-/-}$ mice (n = 12–15). Relevant data values are included in S2 Data. Values are mean ± SD. * $P < 0.05$. WT, wild type.
(PDF)

S9 Fig. ADAMTS13 deficiency does not result in Aβ deposition and synaptic dysfunction in young *APPPS1* mice. (A) Representative micrographs of amyloid plaques labeled with antibody against Aβ in 2-month-old *APPPS1* and *APPPS1–Adamts13*$^{-/-}$ mice. Scale bar, 200 μm. (B–C) Amount of soluble Aβ40 (B) and Aβ42 (C) in 2-month-old *APPPS1* and *APPPS1–Adamts13*$^{-/-}$ mice ($n = 6$). Relevant data values are included in S2 Data. (D) Representative images of Golgi-stained dendritic spines from the hippocampal CA1 region of 2-month-old WT, *Adamts13*$^{-/-}$, *APPPS1*, and *APPPS1–Adamts13*$^{-/-}$ mice. Scale bar, 10 μm. (E) Quantification of spine number per 10 μm of dendrite for each group ($n = 3$). (F) Representative recordings of mEPSCs in hippocampal CA1 neurons from 2-month-old WT, *Adamts13*$^{-/-}$, *APPPS1*, and *APPPS1–Adamts13*$^{-/-}$ mice. Relevant data values are included in S2 Data. (G–H) Summary data showing the frequency (G) and amplitude (H) of mEPSCs from WT, *Adamts13*$^{-/-}$, *APPPS1*, and *APPPS1–Adamts13*$^{-/-}$ mice. $n = 9$ to 10 cells from 3 mice. Relevant data values are included in S2 Data. Values are mean ± SD. ADAMTS13, a disintegrin and metalloprotease with thrombospondin type I motif, member 13; Aβ, amyloid-β; CA1, field CA1 of hippocampus; mEPSC, miniature excitatory postsynaptic current; NS, not significant; WT, wild type.
(PDF)

S10 Fig. ADAMTS13 adeno-associated virus treatment reduces Aβ deposition in *APPPS1* mice. (A and B) Representative micrographs of amyloid plaques labeled with antibody against Aβ (A) and ThS (B) from the cortex and hippocampus of 12-month-old *APPPS1* treated with AAV8-ADAMTS13 or control viruses. Scale bar, 100 μm. AAV8, adeno-associated virus serotype 8; ADAMTS13, a disintegrin and metalloprotease with thrombospondin type I motif, member 13; Aβ, amyloid-β; ThS, thioflavin S.
(PDF)

S11 Fig. Effects of rADAMTS13 on Aβ42 uptake and clearance in astrocytes. (A) Internalization levels of Aβ42 were analyzed by flow cytometry in vehicle- and rADAMTS13-treated astrocytes after incubation with FAM-Aβ42 for 30, 60, and 120 minutes ($n = 3$). (B) Astrocytes were incubated with FAM-Aβ42 for 2 hours, washed, and then incubated FAM-Aβ42–free medium for 2 hours in the presence or absence of rADAMTS13. The residual FAM-Aβ42 was measured by ELISA ($n = 3$). Relevant data values are included in S2 Data. Aβ, amyloid-β; FAM-Aβ42, Aβ1–42 labeled with 5(6)-carboxyfluorescein; rADAMTS13, recombinant ADAMTS13.
(PDF)

S12 Fig. ADAMTS13 AAV treatment restores cognitive function in *APPPS1* mice. (A–B) Number of platform crossings (A) and time spent in the target quadrant in probe trial (B) of the MWM test. (C and D) Total distance traveled (C) and number of rearing (D) in the open-

field test in 12-month-old *APPPS1* treated with AAV8-ADAMTS13 or control viruses. Relevant data values are included in S2 Data. Values are mean ± SD. $n = 13$ to 15 per group; $^{*}P < 0.05$. AAV8, adeno-associated virus serotype 8; ADAMTS13, a disintegrin and metalloprotease with thrombospondin type I motif, member 13; MWM, Morris Water Maze.
(PDF)

S1 Text. A detailed description of methods and materials.
(DOC)

S1 Data. Underlying data for the following Figs 1A, 1B, 1D, 2C, 2D, 2F, 2G, 2H, 3C, 3D, 3F, 4A, 4B, 4D, 4E, 4G, 4H, 4J, 4K, 4L, 4M, 5A, 5B, 5C, 5D, 5E, 5F, 5G, 5J, 5K, 6D, 6E, 6G, 6I, 6K, 7A, 7B, 7C, 7D, 7F, 7H, 7I, 7J, 7K, 7L, 7O and 7P.
(XLSX)

S2 Data. Underlying data for the following S2A, S2C, S3A, S3C, S3D, S3E, S3F, S5B, S6A, S8A, S9B, S9C, S9E, S9G, S9H, S11A, S11B, S12A, S12B, S12C and S12D Figs.
(XLSX)

Acknowledgments

We thank Dr. David M. Holtzman (Department of Neurology, Washington University School of Medicine, St. Louis, MO) for kindly providing the Aβ-stabilizing anti-Aβ antibody HJ5.1.

Author Contributions

Conceptualization: Bing-Qiao Zhao, Wenying Fan.

Data curation: Yongliang Cao, Haochen Xu, Yuanbo Zhu, Mei-Juan Shi, Lixiang Wei, Shuo Cheng, Yiqian Shi, Haiyang Tong, Lijing Kang, Lu Lu, Haiyu Luo, Xing Yang, Xiaofei Bai, Ranran Wang, Yuanyuan Ma.

Formal analysis: Yongliang Cao, Haochen Xu, Yuanbo Zhu, Lixiang Wei, Jin Zhang, Haiyang Tong, Lijing Kang, Lu Lu, Haiyu Luo, Xing Yang, Xiaofei Bai, Ranran Wang, Yuanyuan Ma, Wenying Fan.

Funding acquisition: Bing-Qiao Zhao, Wenying Fan.

Investigation: Yongliang Cao, Haochen Xu, Yuanbo Zhu.

Methodology: Yongliang Cao, Haochen Xu, Yuanbo Zhu, Mei-Juan Shi, Shuo Cheng, Yun Wang, Zhongfeng Wang, Kai Zhong, Bing-Qiao Zhao, Wenying Fan.

Project administration: Bing-Qiao Zhao, Wenying Fan.

Resources: Bing-Qiao Zhao, Wenying Fan.

Software: Yongliang Cao, Yuanbo Zhu, Jin Zhang, Haiyang Tong, Kai Zhong.

Supervision: Bing-Qiao Zhao, Wenying Fan.

Validation: Yongliang Cao, Haochen Xu, Yuanbo Zhu, Yun Wang, Zhongfeng Wang, Kai Zhong.

Visualization: Yongliang Cao, Haochen Xu, Yuanbo Zhu.

Writing – original draft: Yongliang Cao, Haochen Xu, Yuanbo Zhu, Bing-Qiao Zhao, Wenying Fan.

Writing – review & editing: Yongliang Cao, Haochen Xu, Yuanbo Zhu, Bing-Qiao Zhao, Wenying Fan.

References

1. Zlokovic BV. Neurovascular pathways to neurodegeneration in Alzheimer's disease and other disorders. Nat Rev Neurosci. 2011; 12(12):723–38. https://doi.org/10.1038/nrn3114 PMID: 22048062
2. Tarasoff-Conway JM, Carare RO, Osorio RS, Glodzik L, Butler T, Fieremans E, et al. Clearance systems in the brain-implications for Alzheimer disease. Nat Rev Neurol. 2015; 11(8):457–70. https://doi.org/10.1038/nrneurol.2015.119 PMID: 26195256
3. Montagne A, Barnes SR, Sweeney MD, Halliday MR, Sagare AP, Zhao Z, et al. Blood-brain barrier breakdown in the aging human hippocampus. Neuron. 2015; 85(2):296–302. https://doi.org/10.1016/j.neuron.2014.12.032 PMID: 25611508
4. Iturria-Medina Y, Sotero RC, Toussaint PJ, Mateos-Perez JM, Evans AC, Alzheimer's Disease Neuroimaging I. Early role of vascular dysregulation on late-onset Alzheimer's disease based on multifactorial data-driven analysis. Nat Commun. 2016; 7:11934. https://doi.org/10.1038/ncomms11934 PMID: 27327500
5. Albanez S, Ogiwara K, Michels A, Hopman W, Grabell J, James P, et al. Aging and ABO blood type influence von Willebrand factor and factor VIII levels through interrelated mechanisms. J Thromb Haemost. 2016; 14(5):953–63. https://doi.org/10.1111/jth.13294 PMID: 26875505
6. Coppola R, Mari D, Lattuada A, Franceschi C. Von Willebrand factor in Italian centenarians. Haematologica. 2003; 88(1):39–43. PMID: 12551825
7. Quinn TJ, Gallacher J, Deary IJ, Lowe GD, Fenton C, Stott DJ. Association between circulating hemostatic measures and dementia or cognitive impairment: systematic review and meta-analyzes. J Thromb Haemost. 2011; 9(8):1475–82. https://doi.org/10.1111/j.1538-7836.2011.04403.x PMID: 21676170
8. Crawley JT, de Groot R, Xiang Y, Luken BM, Lane DA. Unraveling the scissile bond: how ADAMTS13 recognizes and cleaves von Willebrand factor. Blood. 2011; 118(12):3212–21. https://doi.org/10.1182/blood-2011-02-306597 PMID: 21715306
9. Chauhan AK, Kisucka J, Brill A, Walsh MT, Scheiflinger F, Wagner DD. ADAMTS13: a new link between thrombosis and inflammation. J Exp Med. 2008; 205(9):2065–74. https://doi.org/10.1084/jem.20080130 PMID: 18695007
10. Zheng XL. ADAMTS13 and von Willebrand Factor in Thrombotic Thrombocytopenic Purpura. Annu Rev Med. 2015. 211–25. https://doi.org/10.1146/annurev-med-061813-013241 PMID: 25587650
11. Chion C, Doggen CJM, Crawley JTB, Lane DA, Rosendaal FR. ADAMTS13 and von Willebrand factor and the risk of myocardial infarction in men. Blood. 2007; 109(5):1998–2000. https://doi.org/10.1182/blood-2006-07-038166 PMID: 17053057
12. Andersson HM, Siegerink B, Luken BM, Crawley JTB, Algra A, Lane DA, et al. High VWF, low ADAMTS13, and oral contraceptives increase the risk of ischemic stroke and myocardial infarction in young women. Blood. 2012; 119(6):1555–60. https://doi.org/10.1182/blood-2011-09-380618 PMID: 22110247
13. Matsukawa M, Kaikita K, Soejima K, Fuchigami S, Nakamura Y, Honda T, et al. Serial changes in von Willehrand factor-cleaving protease (ADAMTS13) and prognosis after acute myocardial infarction. Am J Cardiol. 2007; 100(5):760–5.
14. Crawley JTB, Lane DA, Woodward M, Rumley A, Lowe GDO. Evidence that high von Willebrand factor and low ADAMTS-13 levels independently increase the risk of a non-fatal heart attack. J Thromb Haemost. 2008; 6(4):583–8. https://doi.org/10.1111/j.1538-7836.2008.02902.x PMID: 18194418
15. Suidan GL, Brill A, De Meyer SF, Voorhees JR, Cifuni SM, Cabral JE, et al. Endothelial Von Willebrand Factor Promotes Blood-Brain Barrier Flexibility and Provides Protection From Hypoxia and Seizures in Mice. Arterioscler Thromb Vasc Biol. 2013; 33(9):2112–20. https://doi.org/10.1161/ATVBAHA.113.301362 PMID: 23825365
16. Wu YG, Liu W, Zhou Y, Hilton T, Zhao ZL, Liu W, et al. von Willebrand factor enhances microvesicle-induced vascular leakage and coagulopathy in mice with traumatic brain injury. Blood. 2018; 132(10):1075–84. https://doi.org/10.1182/blood-2018-03-841932 PMID: 29941674
17. Xu H, Cao Y, Yang X, Cai P, Kang L, Zhu X, et al. ADAMTS13 controls vascular remodeling by modifying VWF reactivity during stroke recovery. Blood. 2017; 130(1):11–22. https://doi.org/10.1182/blood-2016-10-747089 PMID: 28428179

18. Montine TJ, Koroshetz WJ, Babcock D, Dickson DW, Galpern WR, Glymour MM, et al. Recommendations of the Alzheimer's Disease-Related Dementias Conference. Neurology. 2014; 83(9):851–60. https://doi.org/10.1212/WNL.0000000000000733 PMID: 25080517

19. Montagne A, Zhao Z, Zlokovic BV. Alzheimer's disease: A matter of blood-brain barrier dysfunction? J Exp Med. 2017; 214(11):3151–69. https://doi.org/10.1084/jem.20171406 PMID: 29061693

20. Shang DZ, Zheng XW, Niiya M, Zheng XL. Apical sorting of ADAMTS13 in vascular endothelial cells and Madin-Darby canine kidney cells depends on the CUB domains and their association with lipid rafts. Blood. 2006; 108(7):2207–15. https://doi.org/10.1182/blood-2006-02-002139 PMID: 16597588

21. Zhao BQ, Chauhan AK, Canault M, Patten IS, Yang JJ, Dockal M, et al. vonWillebrand factor-cleaving protease ADAMTS13 reduces ischemic brain injury in experimental stroke. Blood. 2009; 114(15):3329–34. https://doi.org/10.1182/blood-2009-03-213264 PMID: 19687510

22. Jankowsky JL, Fadale DJ, Anderson J, Xu GM, Gonzales V, Jenkins NA, et al. Mutant presenilins specifically elevate the levels of the 42 residue beta-amyloid peptide in vivo: evidence for augmentation of a 42-specific gamma secretase. Hum Mol Genet. 2004; 13(2):159–70. https://doi.org/10.1093/hmg/ddh019 PMID: 14645205

23. Jankowsky JL, Slunt HH, Ratovitski T, Jenkins NA, Copeland NG, Borchelt DR. Co-expression of multiple transgenes in mouse CNS: a comparison of strategies. Biomol Eng. 2001; 17(6):157–65. PMID: 11337275

24. Borchelt DR, Davis J, Fischer M, Lee MK, Slunt HH, Ratovitsky T, et al. A vector for expressing foreign genes in the brains and hearts of transgenic mice. Genet Anal. 1996; 13(6):159–63. PMID: 9117892

25. Chang R, Knox J, Chang J, Derbedrossian A, Vasilevko V, Cribbs D, et al. Blood-Brain Barrier Penetrating Biologic TNF-alpha Inhibitor for Alzheimer's Disease. Mol Pharm. 2017; 14(7):2340–9. https://doi.org/10.1021/acs.molpharmaceut.7b00200 PMID: 28514851

26. McManus RM, Finucane OM, Wilk MM, Mills KH, Lynch MA. FTY720 Attenuates Infection-Induced Enhancement of Aβ Accumulation in APP/PS1 Mice by Modulating Astrocytic Activation. J Neuroimmune Pharmacol. 2017; 12(4):1–12.

27. Wang Y, Liu J, Zhang Z, Wang X, Zhang C. Structure and permeability changes of the blood-brain barrier in APP/PS1 mice: an Alzheimerâ s disease animal model. Neurochem J. 2011; 5(3):220–2.

28. Garcia KO, Ornellas FL, Martin PKM, Patti CL, Mello LE, Frussa-Filho R, et al. Therapeutic effects of the transplantation of VEGF overexpressing bone marrow mesenchymal stem cells in the hippocampus of murine model of Alzheimerâ s disease. Front Aging Neurosci. 2014; 6:30. https://doi.org/10.3389/fnagi.2014.00030 PMID: 24639647

29. Janota C, Brites D, Lemere C, Brito M. Glio-vascular changes during ageing in wild-type and Alzheimers disease-like APP/PS1 mice. Brain Res. 2015; 1620:153–68. https://doi.org/10.1016/j.brainres.2015.04.056 PMID: 25966615

30. Bell RD, Winkler EA, Singh I, Sagare AP, Deane R, Wu Z, et al. Apolipoprotein E controls cerebrovascular integrity via cyclophilin A. Nature. 2012; 485(7399):512–6. https://doi.org/10.1038/nature11087 PMID: 22622580

31. Winkler EA, Nishida Y, Sagare AP, Rege SV, Bell RD, Perlmutter D, et al. GLUT1 reductions exacerbate Alzheimer's disease vasculo-neuronal dysfunction and degeneration. Nat Neurosci. 2015; 18(4):521–30. https://doi.org/10.1038/nn.3966 PMID: 25730668

32. Baek SH, Park SJ, Jeong JI, Kim SH, Han J, Kyung JW, et al. Inhibition of Drp1 Ameliorates Synaptic Depression, Abeta Deposition, and Cognitive Impairment in an Alzheimer's Disease Model. J Neurosci. 2017; 37(20):5099–110. https://doi.org/10.1523/JNEUROSCI.2385-16.2017 PMID: 28432138

33. Kummer MP, Hammerschmidt T, Martinez A, Terwel D, Eichele G, Witten A, et al. Ear2 deletion causes early memory and learning deficits in APP/PS1 mice. J Neurosci. 2014; 34(26):8845–54. https://doi.org/10.1523/JNEUROSCI.4027-13.2014 PMID: 24966384

34. Snyder HM, Corriveau RA, Craft S, Faber JE, Greenberg SM, Knopman D, et al. Vascular contributions to cognitive impairment and dementia including Alzheimer's disease. Alzheimers Dement. 2015; 11(6):710–7. https://doi.org/10.1016/j.jalz.2014.10.008 PMID: 25510382

35. Cirrito JR, Deane R, Fagan AM, Spinner ML, Parsadanian M, Finn MB, et al. P-glycoprotein deficiency at the blood-brain barrier increases amyloid-beta deposition in an Alzheimer disease mouse model. J Clin Invest. 2005; 115(11):3285–90. https://doi.org/10.1172/JCI25247 PMID: 16239972

36. Deane R, Wu ZH, Sagare A, Davis J, Yan SD, Hamm K, et al. LRP/amyloid beta-peptide interaction mediates differential brain efflux of A beta isoforms. Neuron. 2004; 43(3):333–44. https://doi.org/10.1016/j.neuron.2004.07.017 PMID: 15294142

37. Shibata M, Yamada S, Kumar SR, Calero M, Bading J, Frangione B, et al. Clearance of Alzheimer's amyloid-beta(1–40) peptide from brain by LDL receptor-related protein-1 at the blood-brain barrier. J Clin Invest. 2000; 106(12):1489–99. https://doi.org/10.1172/JCI10498 PMID: 11120756

38. Castellano JM, Deane R, Gottesdiener AJ, Verghese PB, Stewart FR, West T, et al. Low-density lipoprotein receptor overexpression enhances the rate of brain-to-blood Abeta clearance in a mouse model of beta-amyloidosis. Proc Natl Acad Sci U S A. 2012; 109(38):15502–7. https://doi.org/10.1073/pnas.1206446109 PMID: 22927427

39. Herring A, Munster Y, Akkaya T, Moghaddam S, Deinsberger K, Meyer J, et al. Kallikrein-8 inhibition attenuates Alzheimer's disease pathology in mice. Alzheimers Dement. 2016; 12(12):1273–87. https://doi.org/10.1016/j.jalz.2016.05.006 PMID: 27327541

40. Ma T, Trinh MA, Wexler AJ, Bourbon C, Gatti E, Pierre P, et al. Suppression of eIF2alpha kinases alleviates Alzheimer's disease-related plasticity and memory deficits. Nat Neurosci. 2013; 16(9):1299–305. https://doi.org/10.1038/nn.3486 PMID: 23933749

41. Zhou Q, Wang M, Du Y, Zhang W, Bai M, Zhang Z, et al. Inhibition of c-Jun N-terminal kinase activation reverses Alzheimer disease phenotypes in APPswe/PS1dE9 mice. Ann Neurol. 2015; 77(4):637–54. https://doi.org/10.1002/ana.24361 PMID: 25611954

42. Richard KL, Filali M, Prefontaine P, Rivest S. Toll-like receptor 2 acts as a natural innate immune receptor to clear amyloid beta(1–42) and delay the cognitive decline in a mouse model of Alzheimer's disease. J Neurosci. 2008; 28(22):5784–93. https://doi.org/10.1523/JNEUROSCI.1146-08.2008 PMID: 18509040

43. Holcomb L, Gordon MN, McGowan E, Yu X, Benkovic S, Jantzen P, et al. Accelerated Alzheimer-type phenotype in transgenic mice carrying both mutant amyloid precursor protein and presenilin 1 transgenes. Nat Med. 1998; 4(1):97–100. PMID: 9427614

44. Arendash GW, King DL, Gordon MN, Morgan D, Hatcher JM, Hope CE, et al. Progressive, age-related behavioral impairments in transgenic mice carrying both mutant amyloid precursor protein and presenilin-1 transgenes. Brain Res. 2001; 891(1–2):42–53. PMID: 11164808

45. Yu M, Chen XW, Liu JH, Ma Q, Zhuo Z, Chen H, et al. Gallic acid disruption of A beta(1–42) aggregation rescues cognitive decline of APP/PS1 double transgenic mouse. Neurobiol Dis. 2019; 124:67–80. https://doi.org/10.1016/j.nbd.2018.11.009 PMID: 30447302

46. Shankar GM, Walsh DM. Alzheimer's disease: synaptic dysfunction and Abeta. Mol Neurodegener. 2009; 4:48. https://doi.org/10.1186/1750-1326-4-48 PMID: 19930651

47. Terry RD, Masliah E, Salmon DP, Butters N, DeTeresa R, Hill R, et al. Physical basis of cognitive alterations in Alzheimer's disease: synapse loss is the major correlate of cognitive impairment. Ann Neurol. 1991; 30(4):572–80. https://doi.org/10.1002/ana.410300410 PMID: 1789684

48. Yao XQ, Jiao SS, Saadipour K, Zeng F, Wang QH, Zhu C, et al. p75NTR ectodomain is a physiological neuroprotective molecule against amyloid-beta toxicity in the brain of Alzheimer's disease. Mol Psychiatry. 2015; 20(11):1301–10. https://doi.org/10.1038/mp.2015.49 PMID: 25917367

49. Izco M, Martinez P, Corrales A, Fandos N, Garcia S, Insua D, et al. Changes in the brain and plasma Abeta peptide levels with age and its relationship with cognitive impairment in the APPswe/PS1dE9 mouse model of Alzheimer's disease. Neuroscience. 2014; 263:269–79. https://doi.org/10.1016/j.neuroscience.2014.01.003 PMID: 24447596

50. Basak JM, Verghese PB, Yoon H, Kim J, Holtzman DM. Low-density Lipoprotein Receptor Represents an Apolipoprotein E-independent Pathway of A beta Uptake and Degradation by Astrocytes. J Biol Chem. 2012; 287(17):13959–71. https://doi.org/10.1074/jbc.M111.288746 PMID: 22383525

51. Sweeney MD, Sagare AP, Zlokovic BV. Blood-brain barrier breakdown in Alzheimer disease and other neurodegenerative disorders. Nat Rev Neurol. 2018; 14(3):133–50. https://doi.org/10.1038/nrneurol.2017.188 PMID: 29377008

52. Sagare AP, Bell RD, Zhao Z, Ma Q, Winkler EA, Ramanathan A, et al. Pericyte loss influences Alzheimer-like neurodegeneration in mice. Nat Commun. 2013; 4:2932. https://doi.org/10.1038/ncomms3932 PMID: 24336108

53. Zlokovic BV. The blood-brain barrier in health and chronic neurodegenerative disorders. Neuron. 2008; 57(2):178–201. https://doi.org/10.1016/j.neuron.2008.01.003 PMID: 18215617

54. Kanekiyo T, Liu CC, Shinohara M, Li J, Bu GJ. LRP1 in Brain Vascular Smooth Muscle Cells Mediates Local Clearance of Alzheimer's Amyloid-beta. J Neurosci. 2012; 32(46):16458–65. https://doi.org/10.1523/JNEUROSCI.3987-12.2012 PMID: 23152628

55. Lam B, Masellis M, Freedman M, Stuss DT, Black SE. Clinical, imaging, and pathological heterogeneity of the Alzheimer's disease syndrome. Alzheimers Res Ther. 2013; 5(1):1. https://doi.org/10.1186/alzrt155 PMID: 23302773

56. Liao F, Hori Y, Hudry E, Bauer AQ, Jiang H, Mahan TE, et al. Anti-ApoE antibody given after plaque onset decreases Abeta accumulation and improves brain function in a mouse model of Abeta amyloidosis. J Neurosci. 2014; 34(21):7281–92. https://doi.org/10.1523/JNEUROSCI.0646-14.2014 PMID: 24849360

57. Yuan Y, Ding Z, Qian J, Zhang J, Xu J, Dong X, et al. Casp3/7-Instructed Intracellular Aggregation of Fe3O4 Nanoparticles Enhances T2 MR Imaging of Tumor Apoptosis. Nano Lett. 2016; 16(4):2686–91. https://doi.org/10.1021/acs.nanolett.6b00331 PMID: 27031226

58. Jin SY, Xiao J, Bao J, Zhou S, Wright JF, Zheng XL. AAV-mediated expression of an ADAMTS13 variant prevents shigatoxin-induced thrombotic thrombocytopenic purpura. Blood. 2013; 121(19):3825–9. https://doi.org/10.1182/blood-2013-02-486779 PMID: 23515928

59. Furman JL, Sama DM, Gant JC, Beckett TL, Murphy MP, Bachstetter AD, et al. Targeting astrocytes ameliorates neurologic changes in a mouse model of Alzheimer's disease. J Neurosci. 2012; 32 (46):16129–40. https://doi.org/10.1523/JNEUROSCI.2323-12.2012 PMID: 23152597

60. Zenaro E, Pietronigro E, Della Bianca V, Piacentino G, Marongiu L, Budui S, et al. Neutrophils promote Alzheimer's disease-like pathology and cognitive decline via LFA-1 integrin. Nat Med. 2015; 21(8):880–6. https://doi.org/10.1038/nm.3913 PMID: 26214837

61. Wang L, Fan W, Cai P, Fan M, Zhu X, Dai Y, et al. Recombinant ADAMTS13 reduces tissue plasminogen activator-induced hemorrhage after stroke in mice. Ann Neurol. 2013; 73(2):189–98. https://doi.org/10.1002/ana.23762 PMID: 23280993

62. Zhu X, Cao Y, Wei L, Cai P, Xu H, Luo H, et al. von Willebrand factor contributes to poor outcome in a mouse model of intracerebral haemorrhage. Sci Rep. 2016; 6:11. https://doi.org/10.1038/s41598-016-0013-4

63. Zhao JJ, Hu JX, Lu DX, Ji CX, Qi Y, Liu XY, et al. Soluble cpg15 from Astrocytes Ameliorates Neurite Outgrowth Recovery of Hippocampal Neurons after Mouse Cerebral Ischemia. J Neurosci. 2017; 37 (6):1628–47. https://doi.org/10.1523/JNEUROSCI.1611-16.2016 PMID: 28069924